Towards a spin-photon interface based on NV centres in an open microcavity

Master Thesis

To obtain the degree of Master of Science
at the Delft University of Technology,
to be defended publicly on Friday June 14, 2024 at 14:00.

C.F.J. Wolfs

Thesis committee:	Prof. Dr. Ir. R. Hanson,	QuTech, Delft University of Technology
	Dr. Ir. T. van der Sar,	Quantum Nanoscience, Delft University of Technology
	Dr. C.K. Andersen,	QuTech, Delft University of Technology
Daily supervisor:	MSc. J. Fischer,	QuTech, Delft University of Technology

TU Delft Delft University of Technology

QuTech

[In physics] everything is a rabbit hole.

Julius Fischer

Abstract

In working towards a quantum internet, nodes based on nitrogen-vacancy (NV) centres in diamond have shown great potential. A key challenge in scaling these networks is the low entanglement generation rate due to low coherent photon emission ($\approx 3\%$) and limited collection efficiency ($\approx 15\%$ using state-of-the-art solid immersion lens setups). Both can be improved by integrating NV centres in an optical cavity. In this thesis NV centres coupled to an open Fabry-Pérot microcavity are investigated. The NV centres are integrated into the cavity by bonding a µm-thin diamond sample to one of the mirrors.

The goal of this thesis is to move towards the realisation of an efficient spin photon interface of NV centres in an open microcavity. To this end, short optical pulses for eventual spin-photon entanglement creation and microwave electronics for spin control are implemented.

A cavity is formed and characterised. A finesse of 3.3×10^3 is found, along with a quality factor of $(3.14 \pm 0.03)\times10^5$ and a mode volume of 83 λ^3. From this, a theoretical outcoupled coherent photon fraction of 14% is determined. NV centres are found in the cavity, and their coupling strength is determined using off-resonant lifetime measurements. From this, the actual outcoupled coherent photon fraction is determined to be (12 ± 1) %. Which represents a more than 25 times improvement over NV centres in solid immersion lenses.

The electron spin resonance (ESR) of an NV centre is measured and a magnetic field strength aligned with its spin axis of (36 ± 1) G is found. A lifetime measurement of an NV centre using pulsed resonant excitation is shown. The last two measurements can be extended to achieve coherent control and resonant readout of the NV spin. Paving the way towards a more efficient spin-photon interface.

Acknowledgments

I owe many people, who were instrumental to the thesis and the experience my gratitude. First and foremost, I would like to thank Julius. I hope it is no secret to you that I enormously enjoyed all our physics discussions. Your passion and enthusiasm was truly what kept me going, it made it so that I was always excited and eager to share results with you. I would also like to thank you for taking me seriously and treating me as an equal. Ronald, thank you for giving me the opportunity of joining your group. I admire how you lead the group and seem to always handle a hundred different things at once. Yanik, you were the one who always kept a cool head in the lab, even when faced with challenges, thank you for your calming presence. I also enjoyed our conversations, you are a great listener. Raymond, thank you for designing the amazing Alice pulse generator and patiently explaining its workings to me.

I want to thank my fellow master students for adding to the experience. Stijn, thank you for finding the hero fibre and for taking my, admittedly bad, jokes so well. Pepijn, thank you for your amazing Inkscape wizardry and of course the Friday joke we bonded over. The other team-diamond master students, Joan, Leo, Constantijn, Caroline, Tobi, Timo thank you for all the nice distractions and discussions I feel like I learned a lot. I also want to thank The other master room students Alex, Kees, Victor, and Sugeiva. Good luck to all of you who have not yet graduated.

Many thanks to my *"fysisch incapabele"* friends. Anna, Fabian, Maaike, Marthe, Meeke, Merel, Milou, Nick, Stein, Stijn, Vlei, Sjors, Wouter. Without you studying physics would not have nearly been so fun. I hope we will remain in close contact. It goes without saying that I could not have been here without support from my family. Even though I can not always make it clear what I am doing, you nonetheless unconditionally support me, thank you Willem, Marieke, Mom and Dad. Last but not least, thank you Esther for always having my back and keeping me sane and grounded.

Cees
Delft, May 2024

Contents

1 Introduction **1**
1.1 Motivation . . . 2

2 Theory **3**
2.1 Nitrogen-Vacancy centre . . . 3
2.2 Optical Cavities & Purcell effect . . . 5
2.2.1 Purcell Effect . . . 6
2.3 Open microcavities . . . 8
2.3.1 Mode spectrum . . . 8
2.3.2 Higher order modes . . . 9
2.3.3 Mode volume . . . 11
2.3.4 Outcoupling . . . 11
2.4 Resonant Excitation . . . 11
2.4.1 Cavity quantum electrodynamics . . . 11
2.4.2 Non-unitary evolution . . . 12

3 Setup and Methods **15**
3.1 Cryogenic open microcavity setup . . . 15
3.1.1 Optical fibre-side setup . . . 17
3.1.2 Optical free space side setup . . . 17
3.1.3 Microwave and electrical control . . . 18
3.2 Short optical pulse setup . . . 20

4 Optical pulse setup characterisation **23**
4.1 Power and stability . . . 23
4.2 Pulse width characterisation . . . 24

5 Characterisation of the open microcavity setup **27**
5.1 Cavity spot characterisation . . . 27
5.2 Vibration level . . . 29

6 Coupling of NV centres to open microcavities **31**
6.1 Detection of NV centres . . . 31
6.2 Purcell enhancement . . . 32
6.3 Optically detected magnetic resonance . . . 33

7 Resonant excitation of NV centres in a cavity **35**
7.1 Photoluminescence excitation . . . 35
7.2 Resonant lifetime measurement . . . 36
7.3 Polarisation suppression . . . 37

8 Conclusion and outlook **39**

A Optical pulse setup **41**
A.1 Electrical wiring of the EOM 41
A.2 Pulse generator. 41

B Impulse response of optical detectors **43**
B.1 Single photon avalanche diode 43
B.2 Superconducting nanowire single photon detector 44

Bibliography **47**

1

Introduction

The internet has arguably been one of the most impactful developments of the last 50 years. Right now a quantum internet [1, 2] is being worked towards. In a quantum internet, the fundamental unit of information is the qubit instead of the classical bit. A qubit can exist in a superposition of the classical bit states. It therefore stores much more information than a classical bit in a different way. Just as at the dawn of the internet it is impossible to predict all eventual applications. However, some important potential applications are already known. These include cryptography secured by the laws of physics [3], as well as distributed quantum computing [4, 5]. One essential building block of a quantum internet is remote entanglement generation where two qubits can be entangled over a long distance. Most feasible protocols use photons as a way to transfer quantum information required to create entanglement remotely. As such a qubit is needed that can coherently transfer its quantum state to a photon.

Colour centres in diamond are specific lattice defects with a localised spin. They have shown promise as quantum internet nodes [6]. Apart from long coherence times, their level structure makes it possible to coherently couple their spin state to an optical wavelength photon. Forming something known as a spin-photon interface. Diamond is an attractive material since it has a large (5.5 eV) bandgap. Colour centers which have their levels within the bandgap are thereby well isolated from electrons in the rest of the diamond. The large abundance of nuclear spin zero ^{12}C means that diamond also does not host a strong nuclear spin bath. Leading to well-isolated stable states. A lot of progress has been made with the nitrogen-vacancy (NV) centre in diamond, here a nitrogen atom exists next to a vacancy in the diamond lattice [7]. Advancements include a multi-node network [8, 9], and metropolitan-scale entanglement [10]. The NV centre has excellent spin properties such as a long coherence time and control over the spin via electric and magnetic fields [11]. The NV centre also allows tuning of emitted photon frequency by electric fields [12].

However, the NV centre has a significant limitation. The emission rate of coherent photons suitable for entanglement generation is low. A breakdown of the reasons for this low rate is shown in Fig. 1.1. The NV generates a photon entangled with its spin state under an optical excitation pulse. The probability of detecting a useful photon per excitation pulse

1

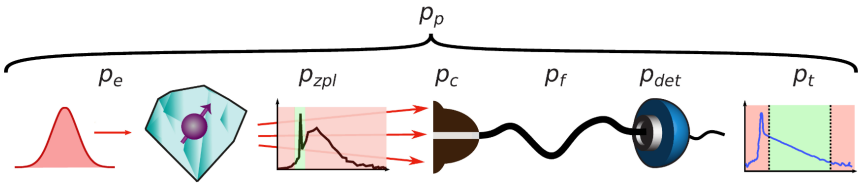

Figure 1.1: Probability to detect a coherent photon per excitation pulse. This is a product of the probability that the excitation pulse excites the emitter is p_e, the probability that the photon is emitted in the ZPL, p_{ZPL}, and subsequently collected into an optical fibre p_c. The probability it is not lost in the fibre p_f. The detector efficiency p_{det} and finally the probability it arrives in the right time-window p_t to allow time-filtering of the excitation light. Adapted from [13].

p_p is low. This is mostly due to only about 3% of the light being emitted as a single photon without additional phonons (p_{zpl}) [14]. As well as limited collection efficiency of photons out of the diamond (p_c). Depending on the entanglement protocol used, the entanglement rate scales either linearly [15, 16], or quadratically with p_p [17]. This limits entanglement generation rates and makes it hard to scale to more than a few nodes.

To overcome this limitation an NV centre can be coupled to a photonic cavity. The zero phonon emission line (ZPL) can then be enhanced by the Purcell effect [18]. Furthermore, the photons couple to the easier to collect cavity mode, enhancing the collection efficiency.

1.1 Motivation

Because of the sensitivity of NV centres to surface electric fields, embedding NV centres in cavity structures embedded within diamond while retaining good optical properties has not yet been demonstrated [19, 20]. Therefore an open microcavity is chosen, where a bulk-like diamond sample is embedded in an external Fabry-Pérot cavity. Cavity-enhanced NV centres have been reported in open microcavities [13, 14, 21], but spin-photon entanglement has remained elusive. The main aim of the thesis is to work towards spin-photon entanglement in an existing cavity setup, paving the way to higher entanglement rates. For this, both spin control and resonant spin readout are required. In this thesis the setup is augmented with the fast control electronics necessary for these. Single-sideband modulation of microwaves is added in preparation for spin control by applying microwave pulses. Spin-photon entanglement creation requires short optical pulses on the timescale of the lifetime. Shorter pulses allow for easier time-filtering, increasing the time window and thereby increasing p_t. This is especially relevant for Purcell-enhanced NV which have shorter lifetimes. A novel pulse setup is implemented, which generates shorter optical pulses than previously used in our group [22].

Chapter 2 introduces the relevant theory about NV centres and cavities. Chapter 3 discusses the microcavity setup used. Chapter 4 presents the characterisation of the novel setup used to generate shorter excitation pulses. Chapter 5 details the cavity formed. Chapter 6 presents Purcell enhancement of NV centres in this cavity. Chapter 7 discusses resonant excitation in the cavity and, finally, chapter 8 concludes the thesis and sketches an outlook.

2

Theory

2.1 Nitrogen-Vacancy centre

The nitrogen-vacancy (NV) centre in diamond is one of the most well-studied colour centres. It consists of a substituted nitrogen atom next to a vacancy in the diamond crystal lattice. This defect leaves five unbonded electrons (two from the nitrogen, and three from the dangling bonds on the carbon atoms neighbouring the vacancy). It can also capture an additional electron from the environment in which case it has six electrons, and is referred to as the negatively charged NV centre (NV^-). The NV^- state is mostly used for quantum information experiments. In the remainder of this thesis, NV refers to the NV^- state unless stated otherwise. The defect exhibits C_{3v} symmetry. From this symmetry four available molecular orbitals can be computed $\{a_1^{'}, a_1\ \ e_x, e_y\}$. The lowest level is in the valence band and is always filled fully. The other three levels lay within the large bandgap (5.5 eV) of diamond. The ground state of NV^- is labelled as $a_1^2e^2$ where the lowest two orbitals are filled and two electrons are in the higher e energy levels. The defect has an excited state ($a_1^1e^3$) where one of the a_1 electrons is excited to the e levels [11]. The energy levels of the NV centre are shown in Fig. 2.1.

Ground state

The lowest energy state is an anti-symmetric combined wave function of one electron in both e_x and e_y ($|e_xe_y - e_ye_x\rangle$) since this state minimises the Coulomb repulsion between the electrons. Pauli's exclusion principle then forces the spin state of the two electrons to be a spin triplet. Under spin-spin interactions the spin-triplet splits further into the degenerate $m_s = \pm 1$ states, and a lower energy $m_s = 0$ state. This causes the NV^- ground state splitting of $D_{gs} = 2.88$ GHz. An external magnetic field splits the $m_s = \pm 1$ degeneracy due to the Zeeman effect. The Hamiltonian for the ground state triplet is given by

$$\mathcal{H}_{gs} = D_{gs}S_z^2 + \gamma_e \vec{S}\cdot\vec{B}, \tag{2.1}$$

where γ_e is known experimentally to be 2.802 MHz/G. After applying a magnetic field either $m_s = +1$ or $m_s = -1$ can be used together with $m_s = 0$ to define a qubit. Where $|0\rangle = |m_s = 0\rangle$ and $|1\rangle = |m_s = -1\rangle$ or $|1\rangle = |m_s = +1\rangle$.

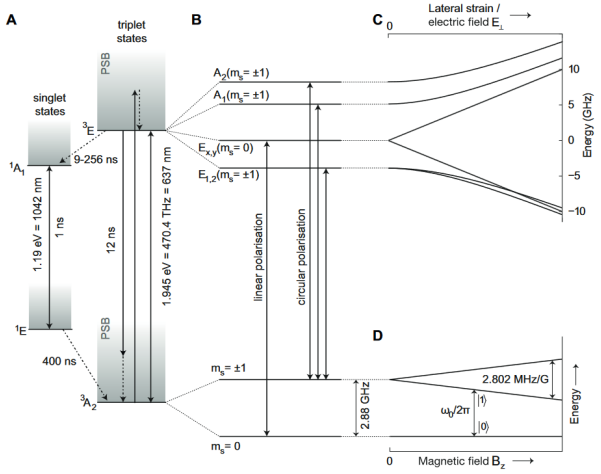

Figure 2.1: Level structure of the NV$^-$ centre. A) shows the singlet and triplet states. B) shows the further splitting of the triplet state due to spin-orbit and Coulomb interactions and the allowed transitions which become observable at cryogenic temperatures. The allowed radiative transitions are spin-preserving. D) shows the splitting off the triplet ground state, due to the Zeeman effect. Typically the $m_s = 0$ and $m_s = -1$ states are used as the qubit subspace. Figure adapted from [23].

Qubit control

The qubit as defined above can be controlled by applying an oscillating magnetic field. This is usually done by applying microwaves. Rabi oscillations between $|0\rangle$ and $|1\rangle$ are induced by microwaves on resonance with the qubit energy splitting ($\omega_0/2\pi$ in Fig. 2.1). The frequency of the oscillations depends on the amplitude of the microwaves. The microwave phase determines the rotation axis on the Bloch sphere. All single qubit operations can be performed using a combination of microwaves and waiting, which rotates the state around the z-axis of the Bloch sphere.

Optical interface

The excited state triplet is 1.945 eV higher in energy than the groundstate, which corresponds to light of 637 nm. Since in the excited state the orbital parts $a_1^1 e_x^2 e_y^1$ and $a_1^1 e_x^1 e_y^2$ are degenerate, the excited state triplet is sixfold degenerate. Under spin-spin and spin-orbit interactions, these states split according to Fig. 2.1. Where $E_{x,y}$ and $E_{1,2}$ are both doubly degenerate. At room temperature, all optical transitions between the ground and excited state are phonon broadened and not separately observable. At cryogenic temperatures the different allowed transitions in Fig. 2.1 B) become observable. The excited state can either decay directly or via the metastable singlet state. Decay over the singlet state is more likely for $m_s = \pm 1$ states. The direct transitions are radiative, emitting photons either with or without accompanied phonons. The zero-phonon process emits light at a wavelength of 637nm and is referred to as the zero phonon line (ZPL). Emission accompanied by phonons occurs in a broader band mostly from 650 nm to 800nm, the phonon sideband (PSB). Excitation of the ground state can occur either resonantly or off-resonantly via higher energy photons over the phonon sideband.

The spin state can be read out selectively by resonantly driving the E_x or E_y transition. Since this excitation is spin-selective excitation only occurs for the $|0\rangle$ state and the relaxation photon will be entangled with the defects' spin state. This spin photon interface can be used to create spin-spin entanglement between two NV centres [24]. Entanglement protocols necessitate indistinguishable photons, therefore only ZPL photons can be used. The Debye-Waller factor (β_0), the ratio of ZPL photons to the total photons emitted, is 2.55% for the NV centre [14]. This is one of the main limiting factors for scaling NV-based networks. The next section discusses how to overcome this limitation using optical cavities.

2.2 Optical Cavities & Purcell effect

A photonic cavity is a structure which acts as a resonator for light. We will treat Fabry-Pérot cavities, consisting of two mirrors a distance L apart. An optical cavity can only confine certain wavelengths of light, others are suppressed by destructive interference after several round trips. Constructive interference occurs for modes of the cavities with a narrow band around the resonance frequencies

$$\nu = q\frac{c}{2nL} = q\nu_{\mathrm{FSR}}, \quad q \in 1, 2, 3... \tag{2.2}$$

with c the speed of light, n the refractive index, q an integer labeling the mode number and ν_{FSR} is the frequency spacing of neighbouring modes (free spectral range). We can calculate the resonance strength at certain frequencies by treating the following model. We consider the left mirror in Fig. 2.2 a) to have reflectivity $R_1 = 1 - T_1$, and the right $R_2 = 1 - T_2$. If we now shine light into the cavity from the left side a part $\sqrt{T_1}$ of the electric field will be transmitted by the left mirror. Light, once it is in the cavity, can make an arbitrary amount of round-trips before it leaves. But the amplitude decreases with each round trip (since the mirrors partially transmit). We can calculate the change in the electric field when making a round trip bouncing of both mirrors

$$g(\omega) = \sqrt{R_1 R_2} e^{-i\frac{\omega 2Ln}{c}}.$$

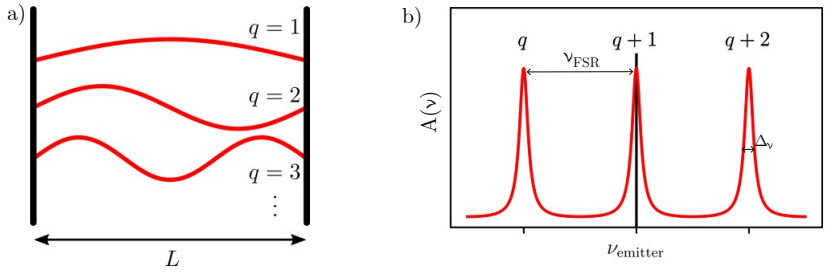

Figure 2.2: Resonances of a simple Fabry-Pérot cavity. a) shows a model cavity with two mirrors opposite to each other, with different resonance modes sketched. b) shows the internal electric field enhancement as a function of input frequency. The frequency spacing ν_{FSR} and linewidth Δ_ν are indicated.

The total internal field is given by the addition of all possible numbers of round-trips, so the total response function of the cavity is given by

$$G(\omega) = \sqrt{T_1}(1 + g(\omega) + g(\omega)^2 + g(\omega)^3 + ...) = \sqrt{T_1}\frac{1}{1-g(\omega)}. \tag{2.3}$$

Where the sum converges since $|g(\omega)| = \sqrt{R_1 R_2} < 1$. The total strength of the resonance is given by the ratio of the internal and incoming electric field intensity:

$$A(\omega) = \frac{I_{\text{cav}}}{I_{\text{inc}}} = \frac{(1-R_1)}{\left(1-\sqrt{R_1R_2}\right)^2 + 4\sqrt{R_1R_2}\sin^2(\frac{2Lc}{n}\omega)}. \tag{2.4}$$

The function is sharply peaked around frequencies for which the sine is zero. These are the mode frequencies given in equation (2.2). The width of the modes depends on the mirror reflectivities. For high reflectivity mirrors ($R_1 \approx 1, R_2 \approx 1$) the cavity mode is narrow and can be modelled well by a Lorentzian. This can be seen by applying a small angle Taylor expansion to the sine. This approximation holds for the cavities considered in this thesis. From the Lorentzian approximation one can extract the full width at half-maximum (FWHM), also called the cavity linewidth

$$\Delta_\omega = \frac{1}{\pi}\frac{1-\sqrt{R_1R_2}}{\sqrt[4]{R_1R_2}}\omega_{\text{FSR}} = \frac{\omega_{\text{FSR}}}{\mathcal{F}}, \tag{2.5}$$

where $\mathcal{F} = \pi\frac{\sqrt[4]{R_1R_2}}{1-\sqrt{R_1R_2}}$ is the cavity finesse. The cavity finesse is a measure of the amount of round-trips a photon makes on average before leaving the cavity. For high-finesse cavities, the approximation

$$\mathcal{F} \approx \frac{2\pi}{1-R_1R_2} = \frac{2\pi}{1-(1-T_1)(1-T_2)} \approx \frac{2\pi}{\mathcal{L}} \tag{2.6}$$

where $\mathcal{L} = T_1 + T_2$ are the total losses in the cavity holds. Losses from the cavity ideally only occur from the mirrors, however additional losses such as scattering losses are often present in experimental realisations. The additional losses lower the finesse

$$\mathcal{F} \approx \frac{2\pi}{\mathcal{L}_{\text{tot}}} = \frac{2\pi}{T_1 + T_2 + \mathcal{L}_{\text{additional}}}.$$

The finesse is purely a function of the total losses and does not depend on the cavity length. An analogous measure called the quality factor (Q) also exists, which is related to the energy lost per oscillation of the electric field. It does depend on the cavity length and is given by $Q = \frac{\omega}{\Delta_\omega} = \frac{\omega}{\omega_{\text{FSR}}}\mathcal{F}$ where ω is the angular resonance frequency of a given mode.

2.2.1 Purcell Effect

When a two-level emitter is coupled to a cavity mode, the emitter's spontaneous emission rate is increased due to the Purcell effect [25]. The cavity opens up a new decay channel for ZPL photons. A ZPL photon can be spontaneously emitted in the cavity mode at a rate Γ_{P} compared to the preexisting rate into free space Γ_{ZPL}. The enhancement of ZPL photons can be quantified by the ZPL Purcell factor

$$F_{\text{P}}^{\text{ZPL}} = \frac{\Gamma_{\text{P}}}{\Gamma_{\text{ZPL}}}. \tag{2.7}$$

The rate for spontaneous emission is given by Fermi's golden rule

$$\Gamma_{e\to g}(\omega) = \frac{2\pi}{\hbar^2}\left|M_{e\to g}\right|^2 D(\omega) = \frac{2\pi}{\hbar^2}\left|\vec{\mu}_{eg}\cdot\vec{E}_{ZPF}\right|^2 D(\omega), \tag{2.8}$$

where the matrix element $M_{e\to g}$ can be computed from the Hamiltonian for the dipole interaction $\mathcal{H} = -\vec{E}\cdot\vec{d}$. It is determined by the overlap of the transition dipole moment ($\vec{d} = \vec{\mu}_{eg}$) and the zero-point electric field. The zero-point or vacuum electric field arises when quantising the electric field in a medium. Upon quantisation, photonic modes become harmonic oscillators which have a non-zero ground state energy even without photons. This residual energy leads to the zero-point electric field

$$\vec{E}_{ZPF} = \left|\vec{E}_{ZPF}\right|\cdot\hat{e} = \sqrt{\frac{\hbar\omega}{2\epsilon_r\epsilon_0 V}}\cdot\hat{e}, \tag{2.9}$$

where $\hat{e}$ is the polarisation direction, ϵ_r the relative permittivity of the medium, ϵ_0 the vacuum permittivity and V the quantisation volume. The emission rate depends on the density of photon states $D(\omega)$. In a homogeneous medium, this is given by

$$D_{hom}(\omega) = \frac{\omega^2 V n^3}{\pi c^3}.$$

For free space emission, the zero-point field polarisation is randomly oriented to the emitter dipole ($\vec{\mu_{eg}} = \mu_{eg}\hat{d}$) averaging $|\hat{d}\cdot\hat{e}|^2$ over all orientations leads to a factor $\frac{1}{3}$. Substituting the above in equation (2.8) gives the unenhanced ZPL rate

$$\Gamma_{ZPL} = \frac{\omega^3 n^3 \mu_{eg}^2}{3\hbar\pi\epsilon_0\epsilon_r c^3}. \tag{2.10}$$

When the electric field is quantised in a cavity one cavity mode corresponds to one bosonic mode, with the same distribution in frequency space as follows from equation (2.4). This means the density of states can be locally very high around the resonance frequencies since the modes are confined in frequency. The density of states for one mode is the Lorentzian:

$$D_{cav}(\omega) = \frac{1}{2\pi}\frac{\Delta_{\omega_c}}{(\omega-\omega_c)^2 + (\Delta_{\omega_c}/2)^2}, \tag{2.11}$$

where ω_c is the resonance frequency of the cavity mode, and Δ_{ω_c} is the width of the mode in frequency space $\Delta_\omega = \frac{\omega_0}{Q}$, which is determined by the cavity quality factor Q. This locally high density of states causes the Purcell effect. Using equation (2.8) and (2.11) the decay rate into the cavity mode Γ_P can be calculated under the assumption of a resonant cavity ($\omega_c = \omega$), substituting this into equation (2.7) gives:

$$F_P^{ZPL} = \frac{\Gamma_P}{\Gamma_{ZPL}} = \frac{|\hat{d}\cdot\hat{e}|^2}{\frac{1}{3}}\frac{D_{cav}(\omega)}{D_{hom}(\omega)} = \frac{6\pi c^3}{n^3}\times\frac{|\hat{d}\cdot\hat{e}|^2}{\omega^3}\times\frac{Q}{V}, \tag{2.12}$$

where $\hat{e}$ is now the polarisation of the cavity mode and V is the appropriate quantisation volume for the cavity mode, the cavity mode volume. In general, for arbitrary ω_c the Purcell

factor is a Lorentzian function of the detuning between the emitter and cavity ($\Delta = \omega - \omega_c$). The main objective of Purcell enhancement is to enhance the fraction of ZPL photons. The PSB transitions of the NV are broad in frequency and effectively not enhanced. The cavity-enhanced ZPL fraction β is given by the branching ratio:

$$\beta = \frac{\Gamma_P}{\Gamma_{PSB} + \Gamma_{ZPL} + \Gamma_P} = \frac{\beta_0 F_P^{ZPL}}{1 + \beta_0 F_P^{ZPL}} \tag{2.13}$$

To maximise the Purcell factor, the quality factor should be maximised and the mode volume minimised. Since the quality factor depends on the Finesse, the losses in the cavity should be minimised.

2.3 Open microcavities

The specific cavity system used is an open microcavity system, where a diamond sample containing NV centres is embedded in an external Fabry-Pérot cavity. The diamond sample is bonded to a planar mirror opposite to an optical fibre which has an embedded spherical dimple mirror [26]. This structure is shown in Fig. 3.1. This section discusses the reasons for and implications of such a structure.

The NV has a permanent electric dipole moment. This makes its excited states first-order sensitive to shifts in electric fields, which can also be seen in Fig.2.1 c). As surfaces exhibit a lot of electric field noise, this can cause NV transition lines to broaden if near surfaces [27]. This makes entanglement generation difficult as indistinguishable photons are needed. This makes nanophotonic cavity structures, such as those often employed with other emitters such as group IV colour centres [28], difficult to use with the NV centre. To use the NV centre in a cavity an open microcavity is employed. The cavities in this thesis consist of one spherical mirror with a certain radius of curvature (ROC) and one planar mirror. A diamond slab is bonded to the planar mirror. The cavity then consists of two media, diamond and air. The vastly different refractive indices cause the diamond-air interface to be partially reflective. This leads to a coupled system of two cavities, one in air and one in diamond.

2.3.1 Mode spectrum

The resonances of the coupled system are given by [19]

$$\upsilon = \frac{c}{2\pi\left(n_a t_a + n_d t_d\right)}\left(q\pi - (-1)^q \arcsin\left(\frac{n_d - n_a}{n_d + n_a}\sin\left(\pi q \frac{n_a t_a - n_d t_d}{n_a t_a + n_d t_d}\right)\right)\right), \tag{2.14}$$

where n_a and n_d are the refractive indices of air and diamond respectively, t_a and t_d are the air gap and diamond thickness respectively, and q is the mode number. The mode spectrum can be seen in Fig. 2.3 a). For a given cavity frequency, the diamond thickness determines whether the electric field is more pronounced in the diamond or air part. Fig. 2.3 c) shows the former, 'diamond-like', mode. For these modes, the mode dispersion is relatively flat. The resonances depend mostly on the diamond thickness and are almost

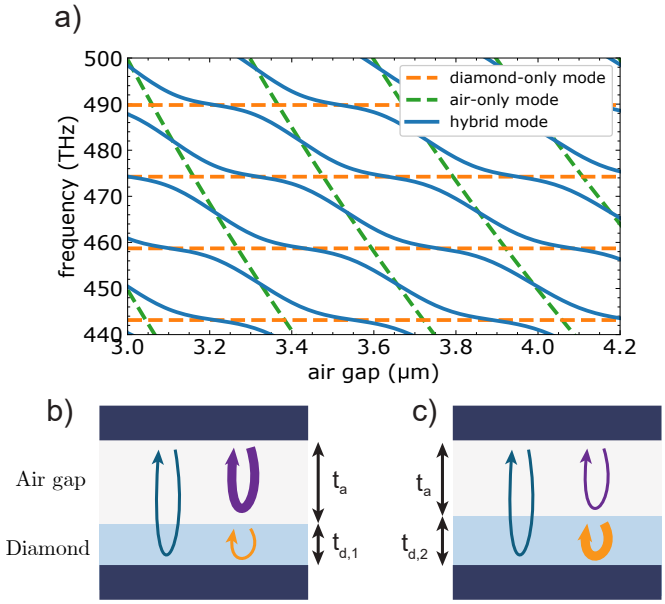

Figure 2.3: a) shows the mode dispersion of an air-diamond cavity for a certain diamond thickness in the solid blue line. Modes near intersections with the dotted orange lines are diamond-like modes. Modes near the intersection with the dotted green line are air-like modes. The diamond thickness determines whether the mode at the NV is air or diamond-like. b) and c) show the relative electric field distribution for an air and diamond-like mode respectively. Images adapted from [21] and [19].

constant with respect to the total cavity length. The latter, 'air-like', mode is shown in Fig. 2.3 b). For these modes the mode profile is steep. Whether the modes at the ZPL frequency of the NV centre are more 'air-like' or 'diamond-like' is purely a function of the diamond thickness, as can be seen in Fig. 2.3 a). In between these two extremes, these modes hybridise forming hybrid modes with mixed properties. To enhance the ZPL emission, in principle 'diamond-like' modes are preferable. The coupling is stronger since the electric field is more contained in the diamond compared to the 'air-like' modes. Furthermore, the flat mode profile makes the system less sensitive to changes in cavity length, which makes the system less sensitive to vibrations. However, the electric field in 'diamond-like' modes has an anti node at the diamond-air interface. This can increase scattering losses, lowering the cavity finesse. These scattering losses depend strongly on the diamond's surface roughness. In practice, operating in 'diamond-like' modes sets stringent constraints on the diamond surface roughness.

2.3.2 Higher order modes

Up until now, a one-dimensional cavity model has been considered. In three dimensions the complex amplitude of the electric field $U(\mathbf{r})$ can be shown to follow the Helmholtz equation

$$\nabla^2 U + k^2 U = 0, \tag{2.15}$$

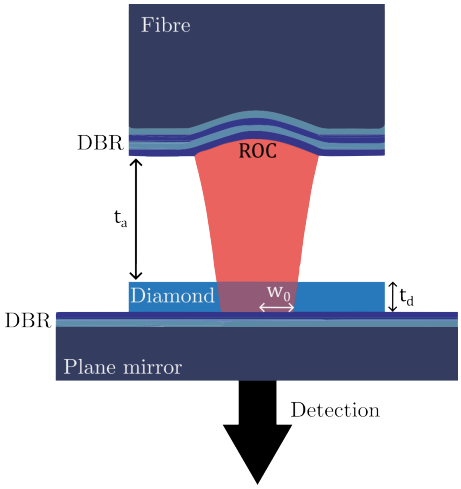

Figure 2.4: Schematic overview of the beam profile in a cavity with one planar and one spherical mirror. The radius of curvature of the spherical mirror is denoted ROC. The mirrors are distributed Bragg reflectors (DBR) and consist of layers of different refractive indices.

with the wave number $k = \frac{\omega}{c}$. Because the mirrors are spherical and planar the paraxial approximation can be made $U(\mathbf{r}) = A(x,y)e^{-ikz}$, assuming the wave travels in the z-direction. Substituting this in equation (2.15) and solving yields an infinite set of solutions indexed by two integers. These are Gaussian-Hermite functions, their exact form can be found here [19]. The mode indexed with both integers zero is called the fundamental mode and is sketched in Fig. 2.4. Other modes present are called higher-order modes. For this thesis, we will always consider the fundamental mode. $U(\mathbf{r})$ for the fundamental mode is given by

$$U(\boldsymbol{r}) \quad = A_0 \frac{w_0}{W(z)} \exp\left(-\frac{\rho^2}{W^2(z)}\right) \exp\left(-ikz - ik\frac{\rho^2}{2R(z)} + i\zeta(z)\right), \tag{2.16}$$

where ρ is the radial distance from the centre of the beam in the transverse plane. A_0 is the electric field amplitude, $W(z)$ is the waist of the beam at position z, and w_0 is the waist of the beam at its most narrow point (at the planar mirror). the Gouy phase $\zeta(z)$, indicates the phase shift between a plane wave and the Gaussian wave. Finally, $R(z)$ is the radius of curvature of the wavefront at position z, they are all specified in literature [19]

At any given z the beam intensity follows a Gaussian in ρ. This is why these modes are also called Gaussian modes. For the cavities considered here with a diamond embedded the beam waist is given by

$$w_0 = \sqrt{\frac{\lambda_0}{\pi n_a}} \sqrt[4]{\left(t_a + \frac{n_a t_d}{n_d}\right)\left(ROC - \left(t_a + \frac{n_a t_d}{n_d}\right)\right)}, \tag{2.17}$$

where t_a and t_d are the air gap and diamond thickness.

2.3.3 Mode volume

The mode volume of a cavity with one spherical and one planar mirror is given by [26]

$$V = \frac{\pi w_0^2}{4L}. \tag{2.18}$$

Embedding the diamond in the cavity changes the effective mode volume. The cavity length L should be replaced with an effective cavity length taking into account the distribution of the electric field [29]:

$$L_{\text{eff}} \equiv \frac{\int_{\text{cav}} \epsilon(z)|E(z)|^2 \, \mathrm{d}z}{\epsilon_0 n_{\text{d}}^2 \left|E_{\text{max,d}}\right|^2 / 2}, \tag{2.19}$$

where $|E_{\text{max,d}}|$ is the maximum electric field amplitude in diamond. For the Purcell factor, it is more effective to minimise the beam waist rather than the cavity length since decreasing the latter will also lower the quality factor.

2.3.4 Outcoupling

Cavities provide not only the possibility for an enhanced ZPL fraction, but also for enhanced collection efficiency. The collection efficiency of NV centres outside a cavity is limited by the random orientation of emitted light and the high index of refraction of diamond. State-of-the-art solid immersion lens setups achieve a collection efficiency of around 15% [30]. The collection efficiency in a cavity is a function of the losses. The probability that a photon exits the cavity through one mirror is given by the ratio of its losses to the total losses. If detection happens on the side of the plane mirror the outcoupling efficiency is given by

$$\text{Outcoupling efficiency} = \frac{\mathcal{L}_{\text{plane}}}{\mathcal{L}_{\text{total}}}, \tag{2.20}$$

so ideally the majority of the losses are associated with the mirror on the side of the detection. The outcoupling efficiency can be multiplied with the cavity ZPL fraction β, equation (2.13), to extract the outcoupled ZPL fraction:

$$\beta_{\text{out}} = \frac{\mathcal{L}_{\text{plane}}}{\mathcal{L}_{\text{total}}}\beta. \tag{2.21}$$

This is the main figure of interest for enhancing entanglement rates.

2.4 Resonant Excitation

To create spin-photon entanglement commonly a short resonant optical excitation pulse is used. The resonant pulse is also known as an optical pi-pulse since it ideally performs a full population inversion from the $m_s = 0$ to the excited state. The following section discusses how an excitation pulse can be modelled in a cavity.

2.4.1 Cavity quantum electrodynamics

As discussed in previous sections, placing an emitter in a cavity effectively opens a new decay channel into the cavity mode. However, it should be noted that this is a symmetric process, in that a photon in the cavity mode can also excite the emitter from the ground state.

The interaction between the emitter and cavity mode comes from the dipole interaction Hamiltonian:

$$\hat{H}^{(I)} = -\hat{\mathbf{d}} \cdot \hat{\mathbf{E}} = \hbar g_c \left(\hat{\sigma}_+ + \hat{\sigma}_-\right)\left(\hat{a_c} + \hat{a_c}^\dagger\right), \tag{2.22}$$

where

$$g_c = \frac{\mu_{eg}}{\hbar}|\vec{E}_{ZPF}||\hat{d}\cdot\hat{e}| = \frac{\mu_{eg}}{\hbar}\sqrt{\frac{\hbar\omega}{2\epsilon_r\epsilon_0 V}}|\hat{d}\cdot\hat{e}|,$$

is the emitter-cavity coupling strength, $\hat{a}_c$ the annihilation operator for photons in the cavity mode, $\hat{e}$ is the polarisation of the cavity mode, μ_{eg} is the transition dipole moment and V the cavity mode volume. The operators $\hat{\sigma_\pm}$ are the raising and lowering operators for the emitter. Using the rotating wave approximation and including terms for the cavity and emitter energy the dynamics can be described by the Jaynes-Cummings Hamiltonian:

$$\hat{H}_{JC} = \hbar\omega_c \hat{a}_c^\dagger \hat{a}_c + \hbar\omega_{eg}|e\rangle\langle e| + i\hbar g_c\left(\hat{\sigma}_+\hat{a}_c - \hat{\sigma}_-\hat{a}_c^\dagger\right). \tag{2.23}$$

The two possible transitions are directly observable in the Hamiltonian, the term $\hat{a}|e\rangle\langle g|$ destroys a photon in the cavity and thereby excites the emitter to the excited state, its hermitian conjugate $\hat{a}^\dagger|g\rangle\langle e|$ does the opposite. In the rotating frame of the emitter, we can define the detuning $\Delta = \omega_c - \omega_{eg}$ and the Hamiltonian simplifies to

$$\hat{H}_{JC} = \hbar\Delta\hat{a}_c^\dagger\hat{a}_c + i\hbar g_c\left(\hat{\sigma}_+\hat{a}_c - \hat{\sigma}_-\hat{a}_c^\dagger\right). \tag{2.24}$$

If the system starts in the state $|e\rangle\otimes|n\rangle$ the only other state accessible is $|g\rangle\otimes|n+1\rangle$ so we can restrict our study to this subspace. For this subspace, the Hamiltonian becomes:

$$H^{(n)} = \hbar\begin{pmatrix} n\Delta & -ig_c\sqrt{n+1} \\ ig_c\sqrt{n+1} & (n+1)\Delta \end{pmatrix} = g_c\sqrt{n+1}\hat{\sigma}_y + (n-\frac{1}{2})\Delta\hat{I} + \frac{1}{2}\Delta\hat{\sigma_z}. \tag{2.25}$$

The eigenstates can be found, they are superpositions of the aforementioned states and are called dressed states. The $\hat{\sigma}_y$ term is of special interest. This will drive Rabi oscillations between $|g\rangle\otimes|n+1\rangle$ and $|e\rangle\otimes|n\rangle$. An excitation will coherently oscillate between the cavity and the emitter. The rate at which this happens is proportional to the square root of the number of photons in the cavity times g_c. These coherent oscillations can be used to excite the emitter. The driving strength depends on the square root of the number of photons in the cavity, resembling the proportionality to the electric field strength.

2.4.2 Non-unitary evolution

To properly simulate time dynamics we also need to consider non-unitary evolution in addition to the Hamiltonian of the previous section. The cavity mirrors have finite transmission values and additional losses exists in the cavity so we need to consider photon loss in the cavity. The loss rate of the cavity can be computed by combining the cavity round trip time and the losses in the cavity. It is related to the linewidth

$$\kappa = \Delta_\omega = 2\pi\Delta_\nu. \tag{2.26}$$

Furthermore, we also need to consider decay of the emitter into other channels than the cavity mode this is given by the unenhanced decay rate Γ. For a two-level system $\Gamma = \frac{1}{\tau}$, where τ is the lifetime of the excited state without any Purcell enhancement. The system with these two decay processes can be modelled by using the Lindbladian formalism. The Lindbladian extends the Schrödinger equation to mixed states by treating the density matrix instead of a pure state. The master equation for the density matrix reads

$$\dot{\rho} = -[\hat{H}, \rho] + \sum_{\mathrm{i}} \gamma_{\mathrm{i}} \left(L_{\mathrm{i}} \rho L_{\mathrm{i}}^{\dagger} - \frac{1}{2} \left\{ L_{\mathrm{i}}^{\dagger} L_{\mathrm{i}}, \rho \right\} \right), \tag{2.27}$$

where L_{i} are jump operators describing the decay processes and γ_{i} are corresponding decay rates. In our case $L_{\mathrm{i}} = \hat{a}, \hat{\sigma}_{-}$ and $\gamma_{\mathrm{i}} = \kappa, \Gamma$.

Weak cavity regime

In the weak cavity regime ($\kappa \gg g_{\mathrm{c}} \gg \Gamma$), also known as the Purcell regime [31], the rate of photon decay is faster than the coherent coupling rate. In this case, coherent oscillations do not occur, as photons decay out of the cavity before they can meaningfully drive the emitter population back. The emitter experiences an enhanced decay rate, and therefore shortened lifetime, in the cavity as found in section 2.2. Assuming a resonant cavity, the ratio of the Purcell enhanced total decay rate to the unenhanced decay rate is given by

$$\frac{\tau}{\tau_{\mathrm{cav}}} = \frac{\Gamma_{\mathrm{P}} + \Gamma}{\Gamma} = 1 + \frac{4 g_{\mathrm{c}}^2}{\kappa \Gamma} = 1 + C, \tag{2.28}$$

where τ_{cav} is the excited state lifetime in the cavity and $C = \beta_0 F_{\mathrm{P}}^{\mathrm{ZPL}}$ is a parameter known as the cooperativity. Open microcavities typically operate in this regime due to the comparatively large mode volume. The Purcell factor and cooperativity can experimentally be determined by measuring the lifetime with and without Purcell enhancement, which can be done by detuning of the cavity mode.

Driving

To perform an optical pi-pulse the emitter can be excited through driving the cavity mode. Under the assumption of a small roundtrip time compared to the cavity decay rate, which is the case for high finesse cavities, we can model the electric field to instantaneously change everywhere in the cavity. We drive the cavity by illuminating one of the mirrors, the input mirror, with a laser of a certain power P_{in}. In the co-rotating frame with the driving frequency the following driving term can then be added

$$i\eta \left(\hat{a}_{\mathrm{c}}^{\dagger} - \hat{a}_{\mathrm{c}} \right),$$

where $\eta = \sqrt{\frac{P_{\mathrm{in}} \kappa_{\mathrm{in}}}{\hbar \omega}}$, is the driving strength given by the square root of the rate of photons hitting the input mirror multiplied by the loss rate of the input mirror. The input mirror loss rate κ_{in} is given by $\kappa \frac{\mathcal{L}_{\mathrm{in}}}{\mathcal{L}_{\mathrm{tot}}}$. Excitation is therefore more efficient from the higher loss side mirror, which agrees with equation (2.4). Assuming the driving is resonant with the transition the final Hamiltonian reads

$$\hat{H} = \hbar \Delta \hat{a}_{\mathrm{c}}^{\dagger} \hat{a}_{\mathrm{c}} + i\eta \left(\hat{a}_{\mathrm{c}}^{\dagger} - \hat{a}_{\mathrm{c}} \right) + i g_{\mathrm{c}} \left(\hat{\sigma}_{+} \hat{a}_{\mathrm{c}} - \hat{\sigma}_{-} \hat{a}_{\mathrm{c}}^{\dagger} \right), \tag{2.29}$$

where Δ is the detuning between the cavity mode and emitter [32, 33]. To simulate pulsed excitation one can vary the input power P_{in} in time.

3

Setup and Methods

3.1 Cryogenic open microcavity setup

The Fabry-Pérot microcavity is constructed by using a single-mode fibre with a spherical dimple mirror opposite to a diamond slab bonded to a coated plane mirror, see Fig. 3.1. A dimple is created on the cleaved fibre tip by laser ablation, afterwards, the coating is applied resulting in a spherical mirror. The coating exists of varying layers of Ta_2O_5 and SiO_2 to form a distributed Braggs reflector (DBR). The plane mirror coating consists of the same two materials. The coating parameters are designed so that the fibre mirror has losses of $\mathcal{L}_{\text{fib}}$ = 50 ppm at λ = 637 nm. The planar mirror has design losses of $\mathcal{L}_{\text{plane}}$ 875 ppm at λ = 637 nm. The radius of curvature of the fibre dimple mirror is 21.4 µm. The planar mirror reflects up to wavelengths of 680 nm. Longer wavelengths are mostly transmitted, ensuring the PSB is still partially collectable. However, since no solid immersion lens is embedded the PSB collection efficiency is low [19]. Embedded in the mirror are three gold striplines, used for microwave driving of the NV centres. These are connected by bondwires to a PCB supplying the microwaves.

As mentioned open microcavities are sensitive to vibrations. To minimise vibrations the cavity is embedded in a cryostat designed to have high vibration stability. It is a floating stage Helium-free optical closed-cycle cryostat with an off-table coldhead (Montana Instruments High Intertia Low Acceleration (HILA)). A drawing of the cryostat can be seen in Fig. 3.2. Inside the radiation shield is the positioning stage containing the fibre and sample mirror. The positioning stage is mounted on the baseplate.

Fibre positioning

The cavity fibre containing the mirror is mounted on a positioning stage (JPE JCPSHR1-a) to allow the fibre to be moved with respect to the sample. This allows the selection of promising cavity locations on the sample and allows the cavity length to be tuned. The positioning stage is equipped with three linear actuators attached to a tripod system that holds the fibre. This three-axis design allows movement in all three dimensions. Additionally, piezo scanning actuators are also included. This allows for fast modulation of the cavity length (on the order of kilohertz). The positioning system is designed to reduce vibrations. It is connected to the cryostat through a vibration isolation stage (JPE CVIP1).

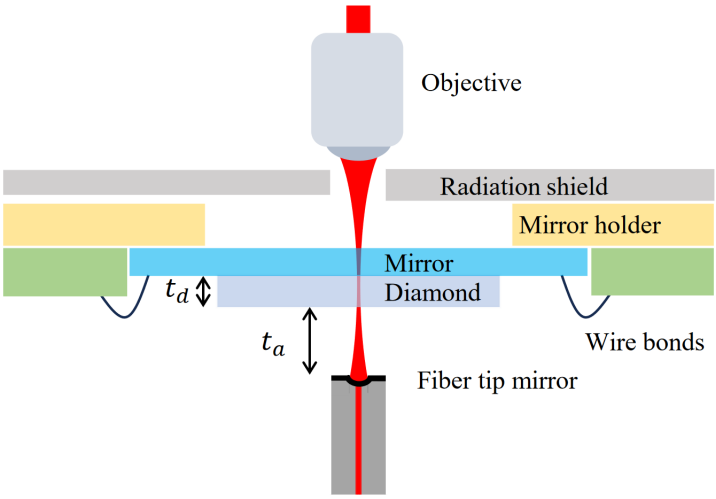

Figure 3.1: Schematic of the open microcavity cryostat. The fibre mirror is located a distance t_a above the diamond sample bonded to the mirror. Microwaves are applied with bond wires to the sample coming from a PCB on the mirror holder. Figure adapted from [34].

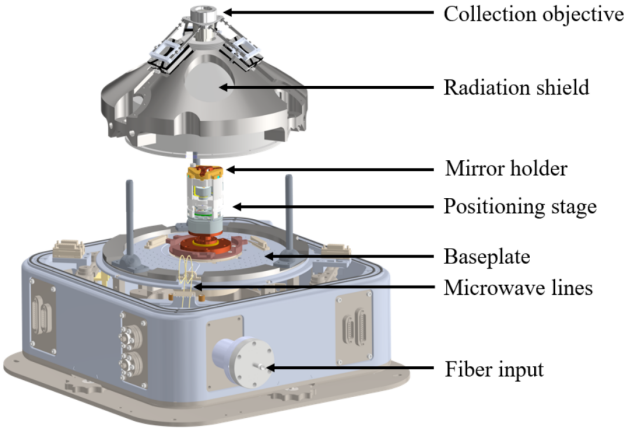

Figure 3.2: Drawing of the cryostat vacuum chamber, the fibre is fed through the fibre feedthrough system into the cryostat leading to the positioning stage. The mirror holder and positioning stage are mounted on the baseplate.

The resonance frequencies of the positioning system and the baseplate of the cryostat are purposely mismatched with each other. This further reduces vibrations.

3.1.1 Optical fibre-side setup

The following sections will discuss the optics used in the setup. Starting with the optics on the fibre-side of the cavity, see Fig. 3.3 a). Laser light is sent to the cavity over the fibre, as this is far less sensitive to alignment. There are four main lasers used in this setup:

1. New Focus Velocity TLB-6300-LN (637 nm, continuous); referred to as cavity check laser
2. Hübner Photonics Cobolt MLD 515 (515 nm, continuous); referred to as off- resonant green laser
3. KT Photonics Katana-05HP (532 nm, pulsed, 230 ps pulse duration, 5-12 MHz repetition rate); referred to as off-resonant pulsed green laser
4. KT Photonics SC-450-2 (450-2000 nm, pulsed, 6 ps pulse duration, 20 MHz repetition rate); referred to as supercontinuum white light source

The cavity check laser allows us to operate a side of fringe lock on the cavity mode. This can be used to compensate for any drifts in the cavity length. The off-resonant green laser is used for continuous off-resonant excitation and with the pulsed green laser lifetime measurements can be performed. The supercontinuum white light source is used to obtain the cavity mode spectrum.

The two green lasers are combined using a 30:70 beamsplitter. The cavity check laser intensity is modulated by an acousto-optic modulator (Gooch and Hoosego FiberQ 633nm). The laser can be modulated by a phase electro-optic modulator (Jenoptik PM635) to create optical sidebands. The laser is then coupled to free space and sent through a linear polariser with a full set of polarisation controls (half-wave plate (HWP) and quarter-wave plate (QWP)) before and after. After, it is combined with the two green lasers using a dichroic mirror (Semrock FF560-FDi0), which transmits light above and reflects light below 560 nm. The combined red and green laser paths are coupled into the input of a 4 × 1 single-mode fibre switch box (Agiltron custom version). The supercontinuum white light source is filtered into a band of 600 nm to 700 nm by a combination of a longpass and shortpass filter. The filtered light is connected to a different input port of the fibre switch box. The switch box allows the selection of one of the inputs to be connected to the output. The output of the switch box is connected to the cavity fibre.

3.1.2 Optical free space side setup

The optics after the plane mirror are mostly free space optics, see Fig. 3.3 c). Since the planar cavity mirror is designed to have higher losses (and thus more efficient outcoupling). The free space side of the cavity is used both for detection and pulsed resonant excitation. Light from the cavity mode is collected with an objective (100x magnification, 0.75 numerical aperture, 4 mm working distance, Zeiss LD EC Epiplan-Neofluar) mounted on a translation stage. A retractable power meter can measure the outcoupled cavity power. A 50:50 pellicle

beamsplitter (Thorlabs BP150) and a corrective lens are positioned on flip mounts, allowing the cavity to be imaged on a camera. Then there are multiple possible paths, depending on the position of mirrors on flip mounts. If the mirror after the beamsplitter (mirror 1) is in the path, the beam is directed either towards a spectrometer (Princeton Instruments SP-2500i) or a free space photodiode, depending on the position of a second flip-mounted mirror (mirror 2). In the photodiode (Thorlabs APD 130A2/M) path, the light is filtered with a 600 nm long-pass filter (Thorlabs FESH0600) to discard any green light transmitted through the cavity. If mirror 1 is retracted a dichroic mirror (Semrock DI 02-P365) is used to separate the PSB and ZPL light. The PSB path is filtered with a long-pass 650 nm and a short-pass 700 nm filter and fibre-coupled into a multimode fibre. The fibre is directed to a single photon avalanche diode (APD). The ZPL path is combined with the resonant excitation path (see section 3.2) using a polarising beamsplitter (PBS) to enable polarisation suppression. After the polarisation optics, a retractable etalon (LightMachinery custom coating) with FWHM $\approx$ 100 GHz to filter the ZPL light is placed on a rotation mount. The rotation mount changes the angle of incidence, allowing tuning of the centre frequency of the etalon. The light is additionally filtered with a 640 nm band-pass filter (Thorlabs FBH640-10, FWHM = 10 nm) and a 600 nm long-pass filter (Thorlabs FESH0600), before it is collected into a single-mode fibre and sent to the APD.

3.1.3 Microwave and electrical control

Fig. 3.4 shows the control electronics. The measurements are coordinated by a real-time microcontroller (Jäger ADwin PRO II). The ADwin has a time resolution of 1 µs. For faster electrical control an arbitrary waveform generator (AWG) is used with a timing resolution of 1.2 Gs/s (Tektronix AWG5014). For time-resolved photon detection, a timetagger (Picoquant Hydraharp 400) is used. To apply microwaves to the sample a vector signal generator (Rohde and Schwarz SMBV100A) is used in combination with a microwave amplifier (Minicircuits ZVE-6W-83+). The AWG is connected to the I and Q ports of the signal generator to enable fast control over the microwave frequency using IQ modulation.

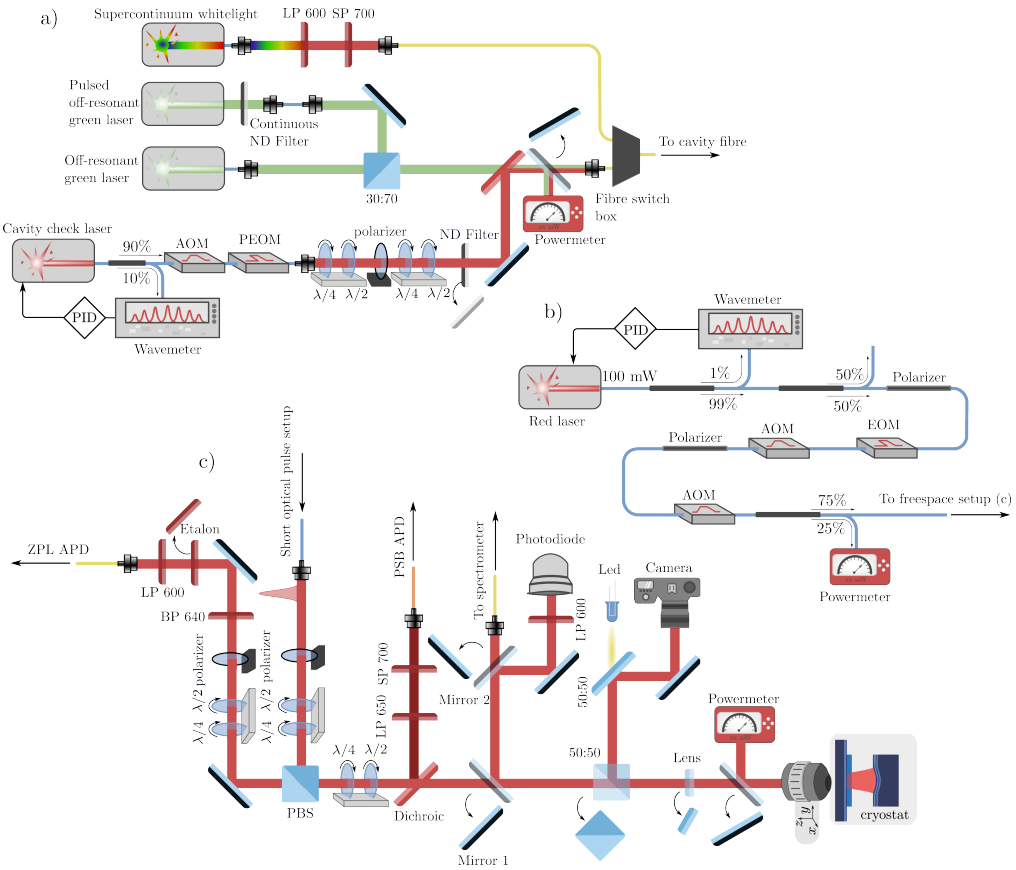

Figure 3.3: The optics used in the setup. The setup consists of three separate parts. The optical fibre-side excitation setup is shown in a). The short optical pulse setup for resonant excitation is shown in b). Lastly c) shows the optical free-space side setup which combines both detection and resonant excitation. Flip-mounts are extensively used to enable many different configurations, depending on the specific experiment being performed.

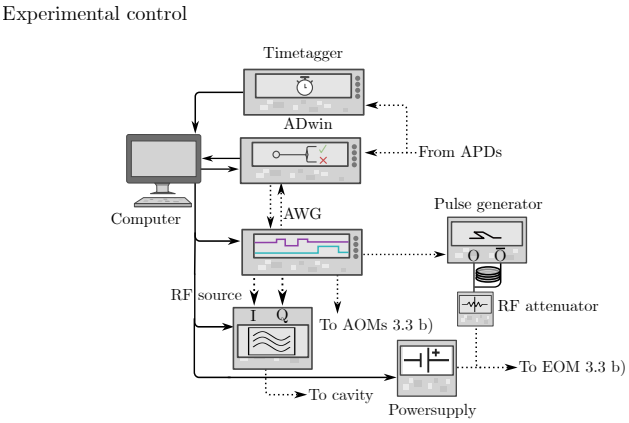

Figure 3.4: Control electronics of the setup. The ADwin PRO II microprocessor orchestrates the measurements. It triggers the AWG to play waveforms for experiments requiring fast control such as resonant excitation. The resonant pulses are generated with a custom pulse generator. The timetagger enables accurate timings of photon detection events.

3.2 Short optical pulse setup

Here, we describe the short optical pulse setup used to generate resonant pulses for the creation of spin-photon entanglement. This setup overcomes a common limitation associated with driving electro-optic modulators (EOMs) for pulse generation.

The short optical pulse setup is shown in Fig. 3.3 b). The important optical elements that generate the pulses are two acousto-optical modulators (AOMs) and an electro-optical modulator (EOM). The laser (Toptica TA-SHG pro) is first attenuated to the maximum input power of the EOM (20 mW). The AOMs (Gooch and Hoosego FiberQ 633nm) have a high on/off ratio of over 50 dB and a rise time of 20ns. Two are used to pre-modulate the laser into pulses with a width of around 50 ns. The EOM (Jenoptik AM635 [35]) has a rise time of 200 ps and is used to shape the fast optical pulse. Depending on the device the on/off ratio is 27-40 dB. The AOMs are required to prevent unwanted excitation by leakage light during the pulse off-time.

Electrical control

The AOMs are driven by two RF drivers (BKT Zepto RF-driver). An AWG (Tektronix 5204) opens and closes the AOMs using the digital input of the drivers. A second, analogue, input of the drivers determines the output power level of the AOMs when open. This input is connected to the ADwin and allows tuning of the pulse power. An EOM modulates optical power as a sinusoidal function of its input voltage, with a period $2V_\pi$. We operate the EOM such that it is normally closed, by DC biasing it in a minimum of the modulation function. It can then briefly be fully opened by applying an electrical pulse with amplitude V_π. Commonly an EOM is electrically controlled with an arbitrary waveform generator (AWG). In this case, typically the AWG bandwidth, not the EOM, limits the shortness of the optical pulse. To overcome this limitation, here the AWG triggers a custom electrical pulse generator. The pulse generated is tunable in width, but not in amplitude. The amplitude of

the electrical pulse generated is 3V, about twice the desired amplitude V_π for the EOM used. There are two strategies to remedy this. For the shortest pulses, the width of the electrical pulse is tuned such that the pulse generator cannot fully open and only reaches V_π in amplitude. For longer pulses a tunable RF attenuator is used. Repetitively pulsing the EOM leads to charging effects, which can shift V_π. To prevent charging every pulse is followed by a negated counterpulse, such that the total applied current is zero. The negated pulse is taken from the inverted output of the pulse generator and delayed using a delay line of 10 meters before it is combined with the original output using an RF combiner. DC biasing is performed with a programmable benchtop power supply (Tenma 13360) connected to the pulse line with a bias tee (Minicircuits ZX85-12G-S+). The wiring is also shown in Fig. 3.4, and more detail is provided in appendix A.

Stability

To eventually ensure high-fidelity pi pulses, the pulse power stability is important. EOMs are sensitive to fluctuations in external conditions, such as the input power and temperature. Therefore it is one of the first elements in the chain, this ensures it always receives the same power directly from the laser. It is also temperature-stabilised at 30 °C using a PID-controlled resistive heating element. Still, V_0 drifts over time. The power meter after the final beamsplitter is used to monitor the EOM leakage. If a significant drift in V_0 is detected the biasing can be optimised automatically. Polarisation fluctuations get converted into power fluctuations by a polariser after the setup. To ensure polarisation stability every element uses polarisation-maintaining (PM) fibre, and fibre polarisers are used in between sensitive elements. To further improve polarisation stability, all optical fibres are tightly taped to the optical breadboard.

4

Optical pulse setup characterisation

This chapter focuses on characterising the optical pulses generated with the setup from the previous chapter and comparing them to a typical quantum network node setup [22]. In section 4.1 the power and polarisation stability of the setup is discussed. Section 4.2 characterises and compares the optical pulses.

4.1 Power and stability

Power and polarisation stability of optical pulses are required for quantum network node applications. Both are necessary to achieve high-fidelity optical pi pulses, power fluctuations can lead to under or over-rotation of the ground to the excited state. Polarisation fluctuations in this setup will be converted to power fluctuations by a free-space polariser after the setup (see Fig. 3.3 c)). The polarisation stability of each element was monitored with a polarimeter. The main elements causing polarisation instability were the two AOMs. Starting from a stable input polarisation (polarisation extinction ratio > 22 dB) a polarisation extinction ratio of 12.4 dB and 12.0 dB was measured, corresponding to polarisation fluctuations of around 7%. A fibre polariser was put in between the AOMs to stabilise the polarisation. The last beamsplitter seems to be slightly polarising, an output polarisation extinction ratio of 18.4 dB was measured.

The maximum usable power output is set by the EOM, specified with a maximum input power of 20 mW and all losses after. Insertion losses occur at fibre-matings and in optical elements. The total optical attenuation of all elements and matings after the EOM was measured to be 10.3 dB, the EOM itself is specified with 7 dB of insertion losses. This results in a maximum usable output power of $\approx 370\,\mu W$ after the last beamsplitter in the setup. The EOM is biased to minimise leakage in between pulses. To quantify the power fluctuations as well as the stability of the EOM bias the power is monitored every second on the power meter in Fig. 3.3 b), such a measurement is shown in Fig. 4.1. The system is stable with maximal power fluctuations on the order of 10 % until 150 minutes after the start of the measurement. There the EOM bias starts to drift away and rebiasing is needed.

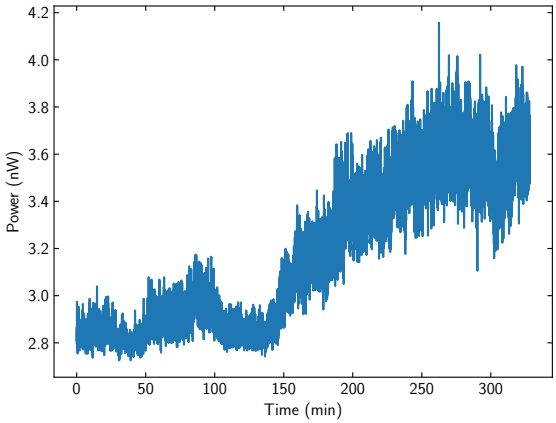

Figure 4.1: Power stability measurement of the optical pulse setup with EOM biased closed.

4.2 Pulse width characterisation

To characterise the generated pulses the output of the optical pulse setup is heavily attenuated and directed to a single photon detector. Due to detector dead time maximally one photon per pulse can be detected. To prevent double-photon errors the pulses are attenuated to a weak coherent pulse leading to less than one detected photon every 20th pulse. A single measurement is averaged over many pulse repetitions. The pulses are triggered with a repetition rate of 200 KHz. The measurements in Fig. 4.2 and 4.3 a) are made using a superconducting nanowire single photon detector (SNSPD). The measurements in Fig. 4.3 b) are obtained using a single photon avalanche diode (Picoquant τ-SPAD).

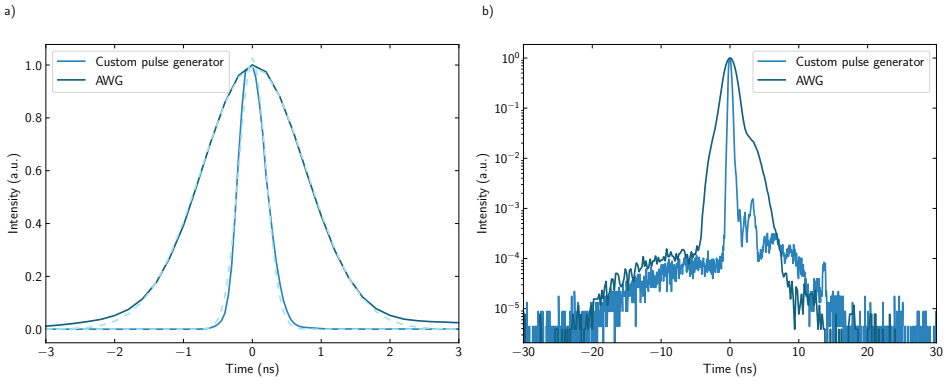

Figure 4.2: A comparison between pulses generated with the AWG directly and using the pulse generator. a) shows the pulses with a Gaussian fit in the light blue dashed line. b) shows the same pulses in a logarithmic scale. In b) both the opening of the AOM and EOM pulse are visible.

Figure 4.2 compares the optical pulse from the setup shown in Fig. 3.3 b) in the configuration without microwave attenuator with the optical pulse used in a previous publication [22], generated by directly controlling the EOM with the AWG. Both were generated using the same EOM. The full width at half maximum (FWHM) is chosen as a figure of interest to compare the pulse widths. This is extracted by fitting a Gaussian to both pulses. These fits are shown as light blue lines in Fig 4.2 a). The fitted FWHM is (457.8 ± 0.2) ps for the pulse generator and (1799 ± 2) ps for the AWG-generated pulse. It should be noted that the impulse response of the SNSPD is not accounted for. This can lead to an overestimation of the width for both pulses, with a more significant effect for shorter pulses. Fig. 4.2 b) shows the same pulses in a logarithmic scale. The AOM opening can also be seen, starting at -20 ns. The pulse generated by the pulse generator shows some artefacts after the pulse. These come from the pulse generator, which has ripples in its settling behaviour. In the AWG-generated pulse two 'shoulders', points where the slope suddenly gets much wider, are visible. These are likely artefacts of the SNSPD impulse response at the chosen bias current, see appendix B for more information.

Tunability

Another advantage of the pulse generator is that, aside from being faster, the pulse width is more tunable than using an AWG. The tunability of the AWG is limited by its sampling rate of 1.2 Gs/s. The pulse generator allows the width of the applied electrical pulse to be set with a precision of about 10ps. This allows for more control over the optical energy in an excitation pulse and could lead to improved optical pi-pulses. Fig. 4.3 a) shows the different applied pulse widths in the configuration without the attenuator, the FWHM is extracted using Gaussian fits. The optical pulse width is tunable in steps of around 30 ps. For longer pulse lengths, the attenuator is needed as otherwise the applied pulse overshoots V_π degrading the quality of the pulse. Fig. 4.3 b) shows pulses made in the configuration with the attenuator, this enables tuning over a larger range. The asymmetry of the pulses in Fig. 4.3 b) is an artefact of the SPAD used. The FWHM is extracted using Gaussian fits, convolved with the impulse response to account for this. More details can be found in appendix B.

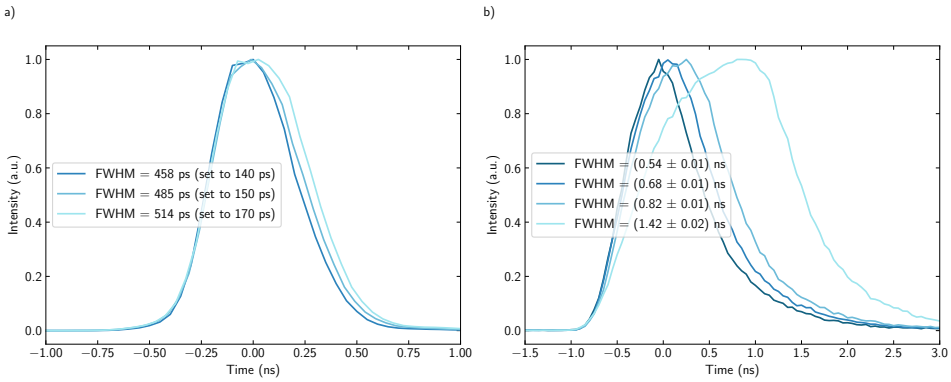

Figure 4.3: Tunability of the temporal width of pulses generated by the pulse generator. a) shows three pulses generated in the configuration without the microwave attenuator captured with an SNSPD. b) shows pulses generated with an attenuator in a larger width range captured on an SPAD. FWHM is extracted with Gaussian fits to each pulse, in b) the detector response is included in the fit.

5

Characterisation of the open microcavity setup

This chapter shows the full characterisation of the cavity used in this thesis. We optimised the lateral position of the cavity for finesse and determined all the relevant parameters. The maximum achievable Purcell factor was also calculated. To this end, the vibration level in the system is also determined.

5.1 Cavity spot characterisation

The fibre positioner allows the fibre to be moved in the plane of the sample, allowing the selection of a particular location to form a cavity. A position close (15 µm) to the stripline is chosen to allow for spin control. The cavity linewidth can be measured by scanning the cavity length using the fibre positioner fine piezo at a high frequency (≈ 3 KHz). During this, the cavity is illuminated using the cavity check and a secondary laser. Both lasers are frequency-stabilised. The transmitted light is detected on a photodiode. In the transmission signal, two Lorentzians can be fitted and converted to frequency using the absolute reference the lasers provide. Linewidth measurements for the cavity spot used in the following chapters are shown in Fig. 5.1. The found linewidth is (1.50 ± 0.01) GHz.

To further determine the cavity parameters, the supercontinuum white laser illuminates the cavity while the cavity length is swept. At every cavity length, a spectrum is taken. All these spectra together are plotted in Fig. 5.2. The fundamental mode resonances can be extracted and fitted with equation (2.14). The air gap length and the diamond thickness are determined from this fit. Together with the linewidth and fibre properties, all relevant properties can then be extracted using the formulas discussed in Chapter 2. For the cavity presented in Fig. 5.1 and 5.2 a diamond thickness of 5.53 µm and air gap of 8.30 µm is found. The quality factor is determined to be $(3.14 \pm 0.03)\times10^5$ and the mode volume 83 λ^3. Assuming perfect dipole overlap and NV placement the Purcell factor is calculated using equation (2.7) to be 21.

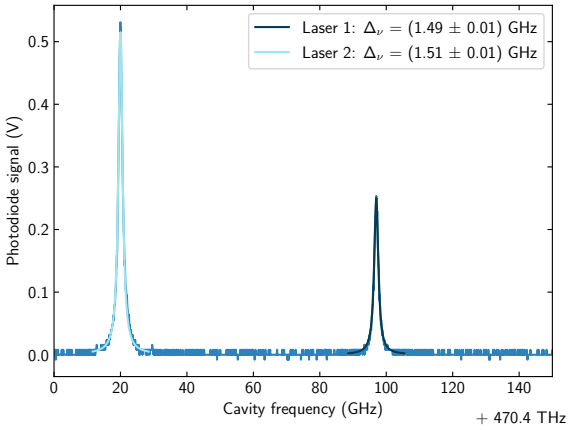

5

Figure 5.1: The transmission signal of two lasers measured while sweeping the cavity length at a piezo scanning frequency of 3546 Hz. This frequency is such that the effect of vibrations on the linewidth can mostly be neglected. The frequency of the two lasers is used to convert displacement to frequency. An averaged linewidth of (1.50 ± 0.01 GHz) is extracted by fitting a Lorentzian to each transmission peak.

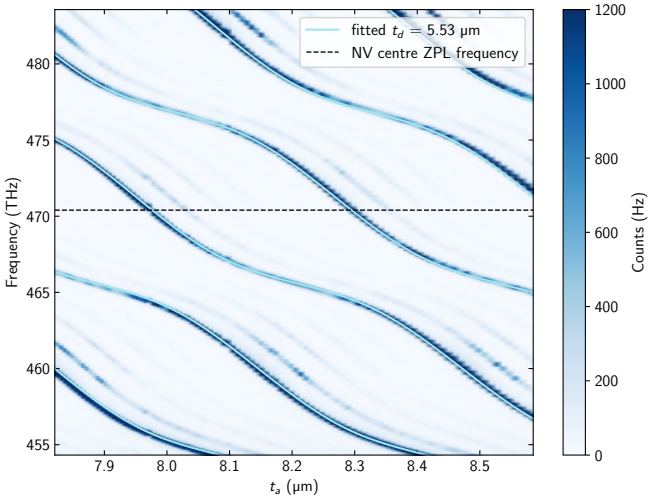

Figure 5.2: Transmission spectra of the cavity at varying air lengths. The fundamental modes are extracted and fitted using (2.14). Higher-order modes are also visible but less prominently than the fundamental mode.

5.2 Vibration level

Open microcavities are by design sensitive to vibrations since the two mirrors can move with respect to each other, shifting the resonance frequency. Vibrations detune the cavity, reducing the spectral overlap with the emitter and thereby reducing the effective Purcell factor. Therefore a low vibration level is essential for achieving good coupling. This has been the main limitation in previous work on the setup [36]. Below the vibration level is quantified to be lower than reported in [36]. To characterise the vibration level the linewidth and cavity length are determined first (more detail is provided in section 5.1). Under illumination with the cavity check laser, the cavity resonance is positioned such that the laser is on the edge of the cavity mode. The transmitted laser power is measured on a photodiode. The photodiode signal is recorded for ten seconds on an oscilloscope (Yokogawa DLM5000 Series Mixed Signal Oscilloscope). Any fluctuations in the cavity length will modulate the cavity transmission since the transmission is a Lorentzian function of the detuning, see equation (2.4). Using the linewidth and mode dispersion slope these power fluctuations are converted to cavity length fluctuations. The vibration level is extracted from a Gaussian fit to the distribution of cavity length detunings. Additionally, the frequency spectrum of the vibrations can be determined by a Fourier transform of the length fluctuations. The standard deviation of the vibration-induced length detunings is found to be 23 pm.

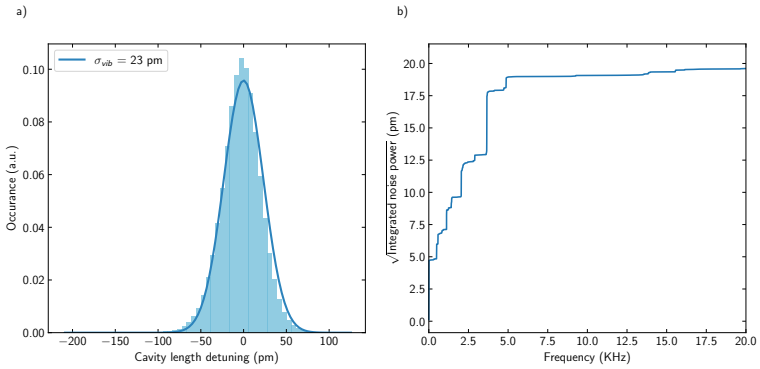

Figure 5.3: Vibration measurement with an acquisition time of ten seconds. a) shows a histogram of all the detunings, the root mean squared vibration level can be extracted from a Gaussian fit to this histogram. b) shows the cumulative power spectral density of the vibrations. A large component of the vibrations occurs near 4 KHz, which corresponds to the resonance frequency of the positioning system.

The vibrations can be taken into account by integrating the Purcell factor at each detuning length over the distribution of vibration-induced detunings in Fig. 5.3 a) [29]. Taking vibrations into account reduces the Purcell factor calculated in section 5.1 from 21 to 14. The finesse at the spot is 3.3×10^3, from this, the total losses can be determined. The out-coupling efficiency determined from the losses using equation (2.20) is 46%. Combining this with the Purcell factor, the outcoupled ZPL fraction is 14%. This presents a 30 times improvement compared to an unenhanced NV centre in a solid immersion lens [14, 30].

6

Coupling of NV centres to open microcavities

In this chapter, we present the coupling of NV centres to an open microcavity. NV centres are detected in section 6.1. Emitter lifetime versus cavity detuning is presented in section 6.2 and the Purcell factor is calculated. Section 6.3 shows an optically detected magnetic resonance measurement with a magnetic field, showing the electron spin resonance of cavity-coupled NV centres

6.1 Detection of NV centres

To find cavity-coupled NV centre transitions the cavity length is swept under off-resonant green laser illumination with 3 mW. The count rate is simultaneously monitored on the ZPL APD. Fig. 6.1 a) shows three clusters of transition lines. The cavity is stabilised and swept finer in Fig. 6.1 b) to obtain a more detailed picture of the clusters. This is done by using a side of fringe lock with the cavity check laser. Locking with the cavity check laser is interspersed with green pulses during which counts are measured. The cavity resonance can then be swept by changing the frequency of the cavity-locking laser. Such a measurement of the middle cluster of Fig. 6.1 a) is shown in Fig. 6.1 b). The cluster consists of two peaks centred around 45 GHz and 55 GHz (+ 470.4 THz). Under off-resonant excitation, the NV spin is preferably prepared in the $m_s = 0$ state. Therefore, the visible transition lines are likely the transitions linking $m_s = 0$ in the ground and excited state E_x and E_y. These are also expected to be coupled most efficiently to the cavity.

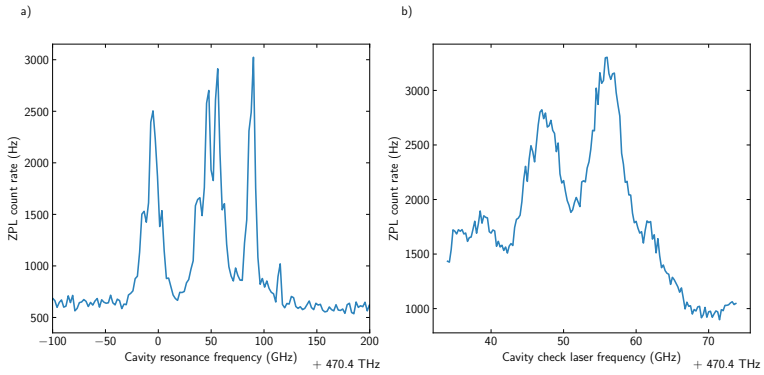

Figure 6.1: Emitters at various cavity resonance frequencies. a) shows ZPL counts while the cavity resonance frequency is swept under 3 mW off-resonant green illumination. b) shows ZPL counts under pulsed green illumination interspersed with pulses of the cavity check laser to enable cavity length stabilisation. a) shows three clusters of NV^- centres. b) shows the middle cluster in more detail.

6.2 Purcell enhancement

In the weak cavity regime, the Purcell effect decreases the lifetime of the excited state. The lifetime reduction is a Lorentzian function of the detuning between the cavity mode and the emitter. We can investigate the Purcell factor achieved in the cavity by measuring the lifetime reduction. The NV centres are off-resonantly excited with the pulsed green laser with 1.8 mW. The counts in the ZPL path are resolved in time using the timetagger, synchronised to the excitation pulses. The cavity resonance is again swept by sweeping the stabilisation laser with a similar procedure as in section 6.1. The lifetime measurements were originally done with the linewidth of 1.50 GHz as measured in Fig.5.1. At some later date, the spot's finesse had degraded, possibly due to damage from high-power laser illumination. The linewidth changed to (2.36 ± 0.02) GHz, as shown in Fig. 7.3. This indicates a decrease in the cavity quality, the Purcell factor is therefore also decreased. Fig. 6.2 shows both lifetime measurement sweeps. There are likely multiple NV centres contributing to the lifetimes at various frequencies, broadening the features. The lowest lifetime detected was (9.05 ± 0.07) ns. The highest lifetime detected was (11.4 ± 0.2) ns with the degraded linewidth. From this a ZPL Purcell factor $F_P^{ZPL} = 8.7 \pm 0.8$ is determined. Note that this is a lower bound since the emitter appears not to be fully detuned at 40 GHz. Assuming a natural lifetime of 12.4 ns, more consistent with literature [22], $F_P^{ZPL} = 12.3 \pm 0.8$ is found. This is (87 ± 6) % of the achievable coupling for this cavity as found in chapter 5. The discrepancy can be explained due to non-ideal NV placement and dipole overlap. Taking this into account the outcoupled ZPL emission is (12 ± 1) %.

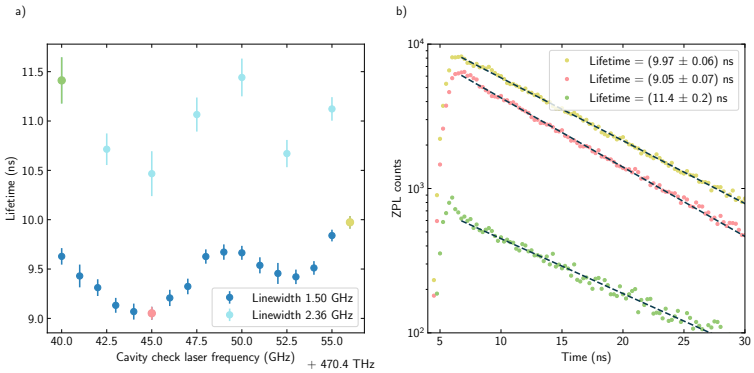

Figure 6.2: Purcell enhancement of the NV centres of Fig. 6.1 b). a) shows lifetime versus detuning at the same cavity spot before and after finesse degradation had taken place. b) shows three of the lifetime measurements along with exponential fits from which the lifetimes are extracted. Corresponding colours in a) and b) show the same lifetime measurement. A lower bound $F_{\mathrm{P}}^{\mathrm{ZPL}} = 8.7 \pm 0.8$ is found comparing the lifetimes.

6.3 Optically detected magnetic resonance

Optically detected magnetic resonance (ODMR) experiments are performed on cavity-coupled NV centres, characterising the electron spin resonance of the NV centres. Here microwaves resonantly drive the spin between $m_{\mathrm{s}} = 0$ and $m_{\mathrm{s}} = \pm 1$ states. During this driving, the NV centres are continually off-resonantly excited, which preferably initialises the NV centre in the $m_{\mathrm{s}} = 0$ state. Since the $m_{\mathrm{s}} = \pm 1$ states are more likely to decay via the relatively long-lived metastable singlet state, not emitting detectable photons for this time, a contrast in brightness can be seen if driving occurs. Sweeping the microwave frequency over the transition frequency then shows a dip in photoluminescence (PL) at the transition frequencies.

Fig. 6.3 shows optically detected magnetic resonance with an applied magnetic field. The experiment presented is done in a cavity made at a different lateral position on the sample than shown in chapter 5. To perform a magnetic resonance experiment microwaves are applied through the striplines in the sample mirror. The microwave frequency is swept using single-sideband modulation under continuous 3 mW green illumination. Each frequency is applied for 10 µs, while the ZPL counts are collected. A magnetic field is applied by attaching a large static magnet outside the cryostat. The cavity is stabilised during the measurement with the stabilisation laser. The $m_{\mathrm{s}} = 0$ to $m_{\mathrm{s}} = -1$ transition is visible at (2.776 ± 0.002) GHz when driving with +30dBm microwave power measured before the cryostat. The $m_{\mathrm{s}} = 0$ to $m_{\mathrm{s}} = +1$ transition was difficult to experimentally see due to increased microwave attenuation of the transmission lines at those frequencies. Still with +35dBm microwave power measured before the cryostat, an indication of a dip was found around 2.977 GHz in Fig. 6.3 b). Using these values in equation (2.1) a magnetic field strength aligned with the quantisation axis of the NV centre of (36 ± 1) G is found. Consistent with the placement of the magnet from simulations of the magnetic field strength and direction.

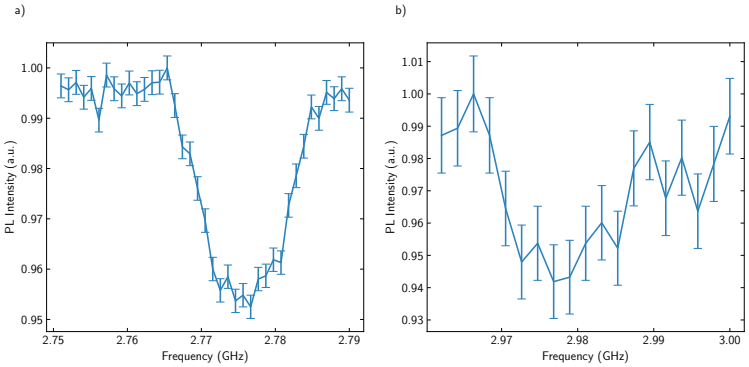

Figure 6.3: Optically detected magnetic resonance (ODMR) of an NV centre in the presence of a magnetic field. a) Photoluminescence (PL) intensity as a function of microwave frequency, showing a dip at the $m_s = 0$ to $m_s = -1$ transition frequency around 2.776 GHz, indicating spin driving at +30 dBm microwave power. b) Indication of a dip corresponding to the $m_s = 0$ to $m_s = +1$ transition around 2.977 GHz at +35 dBm microwave power.

7

Resonant excitation of NV centres in a cavity

Up until now, all excitation was off-resonant. For the use of NV centres as a quantum node, resonant excitation is needed to enable spin-selective readout by driving a single transition. Frequency filtering to filter out excitation light is no longer possible for resonant excitation in the ZPL path. This can be circumvented by using PSB detection, as in section 7.1 and 7.2. However, for entanglement, the ZPL has to be used. In the ZPL detection path polarisation-based filtering is used. Section 7.3 discusses filtering by polarisation suppression in cavities.

7.1 Photoluminescence excitation

Indistinguishable photons are needed for entanglement. This necessitates limited inhomogeneous broadening of the NV transition lines. The sample used showed narrow NV linewidths in previous work [20, 36]. Here we present one photoluminescence excitation (PLE) spectrum to reconfirm the presence of narrow NV transition lines in the current open microcavity setup.

To perform a PLE measurement the cavity check laser is swept while the counts are collected in the PSB path. Counts are collected during a resonant pulse of 40 nW for 200 µs. In between resonant pulses, the off-resonant laser is applied for 10 µs to re-pump the NV^0 centres back to NV^- if ionisation occurred during resonant excitation. To increase the signal-to-noise ratio an additional short-pass filter with a 700 nm cutoff is placed in the PSB path. Fig. 7.1 shows a PLE spectrum from the same cavity as in 6.3. Fig. 7.1 shows four resonant peaks, two of which were fitted with a linewidth of (110 ± 20) MHz and (100 ± 30) MHz respectively. Comparable to previously found on the sample and of related work [21].

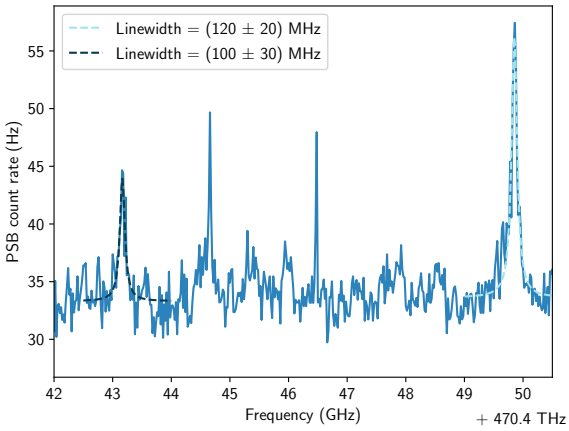

Figure 7.1: Photoluminescence excitation (PLE) spectrum of NV centres. The spectrum shows four resonant peaks, with two peaks fitted with linewidths of (110 ± 20) MHz and (100 ± 30) MHz.

7.2 Resonant lifetime measurement

To show the resonant optical pulses, discussed in Chapter 4, can excite the NV centres a resonant lifetime measurement is performed. The cavity check laser is stabilised at 470.4 THz + 45 GHz and is used to stabilise the cavity with a side of fringe lock. The resonant pulse laser is stabilised at 470.4 THz + 43.5 GHz. A sequence of 100 resonant pulses is applied after which a pulse of 10 µs with 150 µW is applied with the off-resonant green laser to re-pump the NV centres. The counts in the PSB path are resolved with the timetagger, synchronised to the pulses. Fig. 7.2 a) shows two of these measurements, one with and one without the off-resonant pulse. Without off-resonant pulses, the NV centre is expected to ionise or spin-flip and not emit light. This allows the signal-to-noise to be improved by subtracting this measurement from the one with off-resonant light pulses applied. This is necessary because of the large amount of unwanted fluorescence detected.

The subtracted measurement shows an exponential tail after the pulse. The lifetime is extracted from an exponential fit. The lifetime found is (9.7 ± 0.3) ns. This is lower than the (10.4 ± 0.3) ns found in Fig. 6.2 a). As shown in Fig. 7.2 b) a residual excitation pulse is still visible. This suggests the background subtraction was not ideal. Drifts in applied pulse power could have led to different parasitic fluorescence intensities in the background and actual measurements. The error on the lifetime found might be higher due to the non-ideal background subtraction.

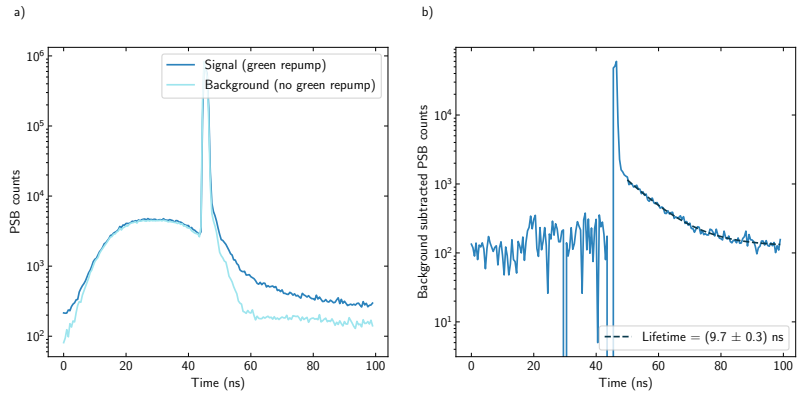

Figure 7.2: Resonant lifetime measurement with PSB detection. a) shows the measurement with and without off-resonant pulses. b) shows the difference of the two traces in a) along with a fitted exponential.

7.3 Polarisation suppression

One of the experimental challenges in all previous sections was low emitter count rates. With off-resonant excitation, we could not drive the NV centres into saturation. We attribute this to inefficient off-resonant excitation. Higher off-resonant powers were not feasible due to the risk of damage to the sample. Resonant excitation with PSB detection suffered from poor detection efficiency in combination with parasitic fluorescence. Resonant excitation combined with resonant detection is needed to move forward, especially in showing spin control. Crucial for this is polarisation suppression. When establishing polarisation suppression at the cavity location discussed in section 5.1 significant polarisation splitting was found. Polarisation splitting causes two orthogonal polarisation modes in the cavity to have different resonance frequencies. This can occur due to birefringence in the diamond [21, 37] and ellipticity in the fibre mirror [19]. Fig. 7.3 shows polarisation splitting of (8.81 ± 0.02) GHz.

To achieve high polarisation suppression ratios with polarisation splitting, the polarisation axis of the beamsplitter is aligned to the polarisation cavity modes. In another configuration, any detuning in the cavity length would rotate the reflected polarisation state, compromising the polarisation suppression. Aligned with the cavity modes we achieve five orders of magnitude polarisation suppression, comparable to similar work [21].

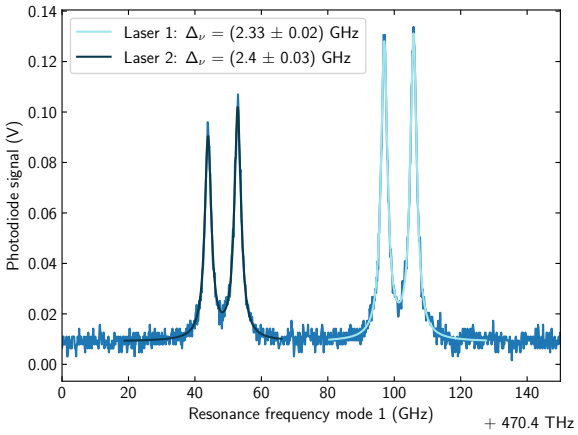

Figure 7.3: Linewidth measurement of the cavity at the same lateral position as Fig. 5.1. The x-axis shows the resonance frequency of the higher frequency mode, here named mode 1. The linewidth has broadened due to the degradation of the cavity. Polarisation splitting of (8.81 ± 0.02) GHz is found.

Polarisation splitting then introduces a challenge for efficient excitation. For optimal Purcell enhancement, one cavity mode will be tuned to be resonant with the enhanced transition. Excitation has to occur in the orthogonal mode, which due to polarisation splitting is off-resonant with the transition being driven. This causes less internal cavity electric field enhancement, see equation (2.4). Furthermore, coherent oscillations to excite the emitter will also be suppressed due to the detuning. This is an especially prevalent concern in optical pi-pulses for spin-photon entanglement as their maximum power is limited. Excitation over an orthogonal polarisation mode can be simulated by introducing a second bosonic mode, representing the orthogonal cavity mode, to equation (2.29) with its own cavity coupling strength.

8

Conclusion and outlook

This thesis contributed towards spin-photon entanglement in an existing open microcavity setup. For this, both spin control and pulsed resonant excitation are required. To this end, the setup was equipped with the necessary fast control electronics. Single-sideband modulation of microwaves was added in preparation for spin control, and a novel pulse setup generating shorter optical pulses than previously used in our group [22] was implemented.

A cavity was formed on the diamond and characterised. A finesse of 3.3×10^3, quality factor of $(3.14 \pm 0.03)\times10^5$ and mode volume 83 λ^3 were found. Taking the vibration level into account the Purcell factor assuming perfect dipole overlap and NV placement is 14. Using off-resonant lifetime measurements and assuming a natural lifetime of 12.4 ns a Purcell factor of 12.3 ± 0.8 is found. The outcoupling efficiency at the cavity location is 46% together with the found Purcell factor this leads to an outcoupled ZPL fraction of (12 $\pm$ 1) %. An over 25 times improvement compared to state-of-the-art solid immersion lens setups with the NV centre [14, 30].

Single-sideband modulation is used to perform an ODMR measurement with an applied static magnetic field. The magnetic field strength aligned with the NV spin-axis is found to be (36 $\pm$ 1) G. This is sufficient to use the NV spin-states as a qubit. The ODMR was performed with square microwave pulses of 10 µs per frequency under continuous off-resonant illumination. This shows fast control over the microwaves applied, which can be extended to microwave pi-pulses and full spin control.

The main limiting factor in this work was low emitter count rates due to inefficient off-resonant excitation and inefficient PSB detection. To use resonant excitation with resonant detection polarisation suppression is required. Polarisation suppression was implemented by aligning to the polarisation axes of the cavity modes and a suppression ratio of five orders of magnitude was achieved. In the cavity, polarisation splitting of the modes of 8.81 GHz, considerably larger than the linewidth, was found. This is an important consideration for spin-photon entanglement as it decreases the effective driving strength of NV-centres, increasing the power required for optical pi-pulses.

The next step is towards spin-photon entanglement is to enable efficient spin readout using resonant detection and excitation. If spin readout is achieved, microwave control should be able to be established, including microwave pi-pulses. In the slightly longer term optical pi-pulses can be used to generate spin-photon entanglement. To achieve this, different cavity locations with less polarisation mode splitting could be investigated. Alternatively, the air gap could be decreased, which could increase the linewidth without compromising the Purcell factor. With the estimated outcoupled ZPL fraction this path paves the way for further more complex experiments, such as spin-spin entanglement at a significantly enhanced rate compared to conventional NV setups.

A

Optical pulse setup

A.1 Electrical wiring of the EOM

The EOM works by virtue of a Mach-Zehnder interferometer. Where a relative phase shift is applied between to the paths by applying a voltage. This is done by applying a voltage to an electrode in the middle of the two beams, while two electrodes on either side are grounded. They internally consist of a material (lithium niobate) whose refractive index depends on the applied electric field. The two paths are therefore phase-shifted differently depending on the strength of the applied electric field, and when combined can either destructively or constructively interfere, depending on the phase difference between the two paths [35].

The combined RF pulse and DC bias signal coming from the bias tee are connected to the middle electrode. The other end of the middle electrode is connected to a DC block and a 50-Ohm terminator. The DC block is used to prevent a constant current due to biasing that heats the electrode.

A.2 Pulse generator

The pulse generator works by using current mode logic (CML), a fast digital logic standard. To generate a tunable digital pulse first two digital pulses of 2.1 ns are generated. This is achieved using two latches with a self-resetting circuit that incorporates a 2.1 ns delay. The trigger of the pulse generator is used as the clock input of the latches, generating the digital pulses.

These two pulses move through an adjustable delay circuit. The delay of both pulses can be set independently, allowing shifting of the pulses with respect to each other. The pulses are combined such that the output is high if and only if the first pulse is high and the second low. The relative delay then determines the width of the output pulse. The delays can be set at around 10ps precision. This setup generates a tunable digital output pulse up to 2.1 ns.

CML logic only has a voltage differential of 800 mV. To convert the digital pulse to an analog pulse with enough voltage swing a fast differential amplifier is used. The amplifier

uses silicon germanium (SiGe) a faster semiconductor than the more conventional silicon due to increased electron mobility.

The pulse generator is optimised for stability. As long as the quality of the trigger pulse is high, meaning it has low jitter, the output pulse will also exhibit low jitter and consistent shape between successive pulses [38].

B

Impulse response of optical detectors

B.1 Single photon avalanche diode

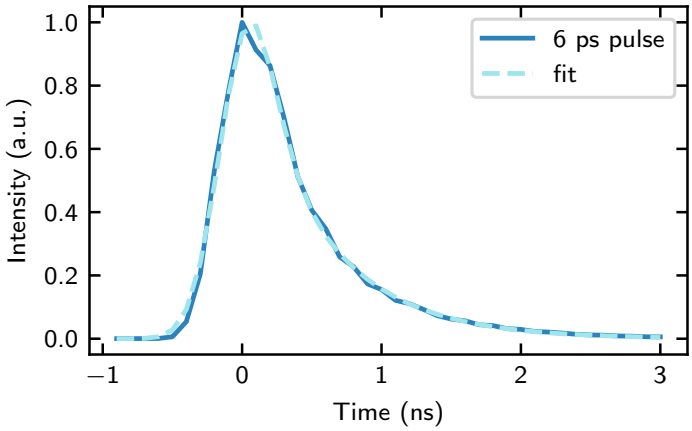

Figure B.1: Impulse response of the single photon avalanche diode used. A custom distribution is fitted.

On the timescale of the optical pulses the impulse response of the SPAD is relevant. To compensate for this the impulse response of the SPAD is determined with the pulsed supercontinuum laser, which produces short pulses of 6 ps. From literature, it is known that SPADs have an exponential decay in the tail of their impulse response function. This arises from the fact that photons may also be absorbed outside the avalanche region, where the liberated electrons have to diffuse to the avalanche region. The diffusion time before the avalanche region is hit follows an exponential distribution [39]. The response of the avalanche region itself can be well approximated by a Gaussian distribution [39]. The time

response for a given photon is either a Gaussian-distributed random variable or the sum of a Gaussian and exponentially distributed random variable. The chosen analytical model for the impulse response is then a weighted sum of a Gaussian distribution with factor p and the same Gaussian distribution convoluted with an exponential distribution with the factor 1 - p. Where p is the fraction of photons that hit the avalanche region directly and do not have to diffuse.

Fig. B.1 shows the super-continuum laser produced pulse resolved using the SPAD (τ-SPAD). With the above described model fitted to it. From the fit the FWHM of the underlying Gaussian distribution is determined to be 0.46 ns ± 0.01 ns. The exponential decay rate of the underlying exponential distribution is found to be 0.56 ns ± 0.03 ns. Compensating for this impulse response is done by numerical convolution of the fitted distribution with a Gaussian distribution for the EOM pulse and fitting this to the observed pulse

B.2 Superconducting nanowire single photon detector

To investigate the detector response of the nanowire detectors used for imaging the pulses we used the off-resonant pulses laser with a known pulse width (FWHM) of 230 ps. Counts are synchronised to the laser trigger and imagined on a timetagger. Fig. B.2 shows the response of the nanowires averaged over many pulses. As can be seen in the figure the temporal width of the response function strongly depends on the bias current applied in the nanowires. The AWG-generated pulse shown in Fig. 4.2 was obtained with the nanowire biased with 7.5 µA [22]. The same 'shoulder' points described in the main text are also visible on the 230 ps pulse biased at this point. For higher bias currents this feature is less prominent. This is therefore likely an artefact of the nanowire system response at a particular bias point. The highest bias point was found to have the shortest system response. This was therefore used in imaging the pulses from the novel setup described in the main text.

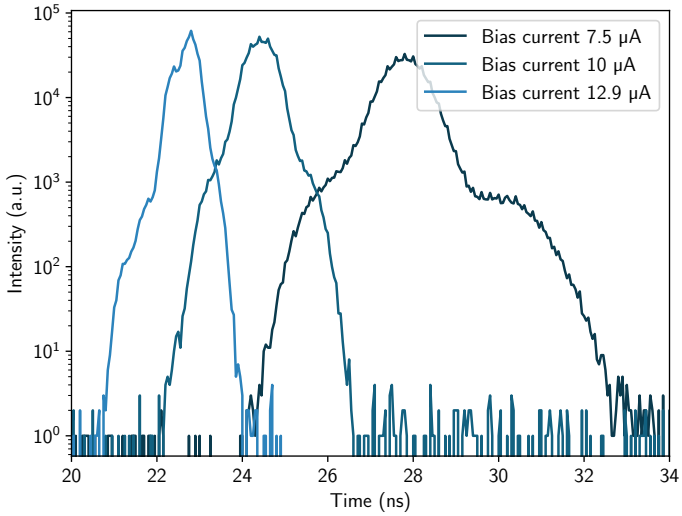

Figure B.2: Response of a superconducting nanowire single photon detector to a 230 ps (FWHM) pulse at three different bias current setpoints. Higher bias points show significantly shorter system jitter and less delay.

Bibliography

References

[1] H Jeff Kimble. The quantum internet. *Nature*, 453(7198):1023–1030, 2008.

[2] Stephanie Wehner, David Elkouss, and Ronald Hanson. Quantum internet: A vision for the road ahead. *Science*, 362(6412):eaam9288, 2018.

[3] Artur Ekert and Renato Renner. The ultimate physical limits of privacy. *Nature*, 507(7493):443–447, 2014.

[4] Liang Jiang, Jacob M Taylor, Anders S Sørensen, and Mikhail D Lukin. Distributed quantum computation based on small quantum registers. *Physical Review A*, 76(6):062323, 2007.

[5] Anne Broadbent, Joseph Fitzsimons, and Elham Kashefi. Universal blind quantum computation. In *50th annual IEEE symposium on foundations of computer science*, pages 517–526. IEEE, 2009.

[6] Maximilian Ruf, Noel H. Wan, Hyeongrak Choi, Dirk Englund, and Ronald Hanson. Quantum networks based on color centers in diamond. *Journal of Applied Physics*, 130(7):070901, August 2021. Number: 7.

[7] Fedor Jelezko and Jörg Wrachtrup. Single defect centres in diamond: A review. *Physica Status Solidi (a)*, 203(13):3207–3225, 2006.

[8] Matteo Pompili, Sophie LN Hermans, Simon Baier, Hans KC Beukers, Peter C Humphreys, Raymond N Schouten, Raymond FL Vermeulen, Marijn J Tiggelman, Laura dos Santos Martins, Bas Dirkse, et al. Realization of a multinode quantum network of remote solid-state qubits. *Science*, 372(6539):259–264, 2021.

[9] SLN Hermans, Matteo Pompili, HKC Beukers, Simon Baier, Johannes Borregaard, and Ronald Hanson. Qubit teleportation between non-neighbouring nodes in a quantum network. *Nature*, 605(7911):663–668, 2022.

[10] Arian J Stolk, Kian L van der Enden, Marie-Christine Slater, Ingmar te Raa-Derckx, Pieter Botma, Joris van Rantwijk, Benjamin Biemond, Ronald AJ Hagen, Rodolf W Herfst, Wouter D Koek, et al. Metropolitan-scale heralded entanglement of solid-state qubits. *arXiv preprint arXiv:2404.03723*, 2024.

[11] Marcus W Doherty, Neil B Manson, Paul Delaney, Fedor Jelezko, Jörg Wrachtrup, and Lloyd CL Hollenberg. The nitrogen-vacancy colour centre in diamond. *Physics Reports*, 528(1):1–45, 2013.

[12] Ph Tamarat, T Gaebel, JR Rabeau, M Khan, AD Greentree, H Wilson, LCL Hollenberg, S Prawer, P Hemmer, F Jelezko, et al. Stark shift control of single optical centers in diamond. *Physical Review Letters*, 97(8):083002, 2006.

[13] M.T. Ruf. *Cavity-enhanced quantum network nodes in diamond.* PhD thesis, Delft University of Technology, 2021.

[14] Daniel Riedel, Immo Söllner, Brendan J. Shields, Sebastian Starosielec, Patrick Appel, Elke Neu, Patrick Maletinsky, and Richard J. Warburton. Deterministic Enhancement of Coherent Photon Generation from a Nitrogen-Vacancy Center in Ultrapure Diamond. *Physical Review X*, 7(3):031040, September 2017. Number: 3.

[15] Earl T Campbell and Simon C Benjamin. Measurement-based entanglement under conditions of extreme photon loss. *Physical Review Letters*, 101(13):130502, 2008.

[16] Norbert Kalb, Andreas A Reiserer, Peter C Humphreys, Jacob JW Bakermans, Sten J Kamerling, Naomi H Nickerson, Simon C Benjamin, Daniel J Twitchen, Matthew Markham, and Ronald Hanson. Entanglement distillation between solid-state quantum network nodes. *Science*, 356(6341):928–932, 2017.

[17] Sean D Barrett and Pieter Kok. Efficient high-fidelity quantum computation using matter qubits and linear optics. *Physical Review A*, 71(6):060310, 2005.

[18] Erika Janitz, Mihir K. Bhaskar, and Lilian Childress. Cavity quantum electrodynamics with color centers in diamond. *Optica*, 7(10):1232, October 2020. Number: 10.

[19] Suzanne B van Dam, Maximilian Ruf, and Ronald Hanson. Optimal design of diamond-air microcavities for quantum networks using an analytical approach. *New Journal of Physics*, 20(11):115004, November 2018. Number: 11.

[20] Maximilian Ruf, Mark IJspeert, Suzanne Van Dam, Nick De Jong, Hans Van Den Berg, Guus Evers, and Ronald Hanson. Optically coherent nitrogen-vacancy centers in micrometer-thin etched diamond membranes. *Nano Letters*, 19(6):3987–3992, 2019.

[21] Viktoria Yurgens. *Cavity-enhancement of a low-noise single-photon emitter in diamond.* PhD thesis, University of Basel, 2023.

[22] SLN Hermans, Matteo Pompili, L Dos Santos Martins, A RP Montblanch, HKC Beukers, Simon Baier, Johannes Borregaard, and Ronald Hanson. Entangling remote qubits using the single-photon protocol: an in-depth theoretical and experimental study. *New Journal of Physics*, 25(1):013011, 2023.

[23] Hannes Bernien. *Control, measurement and entanglement of remote quantum spin registers in diamond.* PhD thesis, Delft University of Technology, 2014.

[24] Hannes Bernien, Bas Hensen, Wolfgang Pfaff, Gerwin Koolstra, Machiel S Blok, Lucio Robledo, Tim H Taminiau, Matthew Markham, Daniel J Twitchen, Lilian Childress, et al. Heralded entanglement between solid-state qubits separated by three metres. *Nature*, 497(7447):86–90, 2013.

[25] Edward Mills Purcell. Spontaneous emission probabilities at radio frequencies. In *Confined Electrons and Photons: New Physics and Applications*, pages 839–839. Springer, 1995.

[26] D Hunger, T Steinmetz, Y Colombe, C Deutsch, T W Hänsch, and J Reichel. A fiber Fabry–Perot cavity with high finesse. *New Journal of Physics*, 12(6):065038, June 2010. Number: 6.

[27] Andrei Faraon, Charles Santori, Zhihong Huang, Victor M Acosta, and Raymond G Beausoleil. Coupling of nitrogen-vacancy centers to photonic crystal cavities in monocrystalline diamond. *Physical Review Letters*, 109(3):033604, 2012.

[28] Carlo Bradac, Weibo Gao, Jacopo Forneris, Matthew E Trusheim, and Igor Aharonovich. Quantum nanophotonics with group iv defects in diamond. *Nature communications*, 10(1):5625, 2019.

[29] Suzanne B Van Dam, Maximilian Ruf, and Ronald Hanson. Optimal design of diamond-air microcavities for quantum networks using an analytical approach. *New Journal of Physics*, 20(11):115004, 2018.

[30] Bas Hensen, Hannes Bernien, Anaïs E Dréau, Andreas Reiserer, Norbert Kalb, Machiel S Blok, Just Ruitenberg, Raymond FL Vermeulen, Raymond N Schouten, Carlos Abellán, et al. Loophole-free bell inequality violation using electron spins separated by 1.3 kilometres. *Nature*, 526(7575):682–686, 2015.

[31] Andreas Reiserer and Gerhard Rempe. Cavity-based quantum networks with single atoms and optical photons. *Reviews of Modern Physics*, 87(4):1379, 2015.

[32] Alp Sipahigil, Ruffin E Evans, Denis D Sukachev, Michael J Burek, Johannes Borregaard, Mihir K Bhaskar, Christian T Nguyen, Jose L Pacheco, Haig A Atikian, Charles Meuwly, et al. An integrated diamond nanophotonics platform for quantum-optical networks. *Science*, 354(6314):847–850, 2016.

[33] Yanik Herrmann, Julius Fischer, Julia M Brevoord, Colin Sauerzapf, Leonardo GC Wienhoven, Laurens J Feije, Matteo Pasini, Martin Eschen, Maximilian Ruf, Matthew J Weaver, et al. Coherent coupling of a diamond tin-vacancy center to a tunable open microcavity. *arXiv preprint arXiv:2311.08456*, 2023.

[34] Stijn Scheijen. Cavity-enhanced coherent emission of nitrogen-vacancy centers in diamond, 2024. Master thesis, Delft University of Technology.

[35] JENOPTIK Optical Systems GmbH, Jena, Germany. *Integrated-optical modulators*, 1st edition, June 2018. Available at https://www.jenoptik.com/products/optoelectronic-systems/light-modulation/integrated-optical-modulators-fiber-coupled.

[36] M. Ruf, M.J. Weaver, S.B. van Dam, and R. Hanson. Resonant Excitation and Purcell Enhancement of Coherent Nitrogen-Vacancy Centers Coupled to a Fabry-Perot Microcavity. *Physical Review Applied*, 15(2):024049, February 2021. Number: 2.

[37] Jonathan Körber, Maximilian Pallmann, Julia Heupel, Rainer Stöhr, Evgenij Vasilenko, Thomas Hümmer, Larissa Kohler, Cyril Popov, and David Hunger. Scanning cavity microscopy of a single-crystal diamond membrane. *Physical Review Applied*, 19(6):064057, 2023.

[38] Raymond Vermeulen. Pulse generator and method for generating pulses, 2022. NL2027170B1.

[39] NR Das and M Jamal Deen. Low-bias performance of avalanche photodetector. a time-domain approach. *IEEE journal of quantum electronics*, 37(1):69–74, 2001.